Orogen-Parallel Transition From a Decoupled Fore-Arc Sliver to Andean-Type Mountain Chain: Paleomagnetic and Geologic Evidence From Southern Chile (37–39°S)

Gaia Siravo[1] , **Fabio Speranza[1]** , **Catalina Hernandez-Moreno[1,2]** , and **Anita Di Chiara[1,3]**

[1]Istituto Nazionale di Geofisica e Vulcanologia, Rome, Italy, [2]Now at Tecnologias Avanzadas Inspiralia SL, Madrid, Spain, [3]Now at Scripps Institution of Oceanography, La Jolla, CA, USA

Abstract The Chiloé fore-arc sliver is an approximately N-S elongated crust block detached from South America along the dextral intra-arc Liquiñe-Ofqui fault zone (LOFZ). The sliver is internally dissected by active NW-SE sinistral faults whose relations with the LOFZ are speculative, also due to widespread fluvioglacial and volcanic blanket hiding the substratum. We focus on the northern LOFZ end and on the Biobio fault, supposedly the northernmost of the sinistral fault set, reporting on the results from field investigation and paleomagnetism of 48 (mostly Oligo-Miocene) volcanic sites. We find that the Biobio fault is an old inherited crust discontinuity that did not yield significant block rotation and deformation during the Cenozoic, thus testifying the end of sinistral shear at about 38°S. At the same latitudes, a northward transition from pure strike-slip to transpressive LOFZ deformation occurs. Intense tectonic deformation and >90° clockwise rotations characterize the main LOFZ strand. Conversely, a supposedly western LOFZ strand displays counterclockwise rotations, similar to the pattern previously documented in the forearc; thus, it does not represent a LOFZ segment. LOFZ and sinistral fault kinematics must be related, and we suggest that crust pushed northward west of the LOFZ escapes laterally toward the trench along the sinistral faults. We also speculate that the northward increasing age of the subducting Nazca plate implies a concomitant decrease of heat transfer on the upper plate, thus an increasing crust rigidity that eventually inhibits strain partitioning and sliver decoupling from 38°S.

1. Introduction

Fore-arc slivers occur in active convergent margins where oblique subduction and/or ridge collision is fully partitioned into dip-slip compressional deformation—taking place along megathrust faults—and margin parallel strike-slip shear. Crust slivers undergo drift as they are displaced along regional-scale strike-slip faults parallel to the trench, which may be newly formed or reactivated (Nelson et al., 1993) and usually follow the hot and weak crust that surrounds volcanic arcs (Beck, 1980; Dewey & Lamb, 1992; Wallace et al., 2004).

Present-day fore-arc sliver motion can be constrained by earthquake slip vectors—revealing instantaneous crust displacements—and GPS velocity field data that however are based on an observation window surely smaller than a complete seismic cycle (e.g., McCaffrey, 2008). At most subductions zones, the GPS velocity field is dominated by the coseismic and postseismic signals from the subduction megathrust earthquakes (e.g., Wang et al., 2012), implying that it can be hardly used to unravel sliver motion and its internal permanent deformation over geological times. On the other hand, the long-term deformation history of crust is classically determined with geologic-tectonic or geophysical evidence, for instance, geological maps and sections, kinematic indicators on fault planes, or results of seismic reflection and refraction investigations. However, bedrock units useful to untangle geological deformation can be hidden by glacial and volcanic blanket, thick soil, and vegetation. In such cases, paleomagnetic data from scattered bedrock exposures can represent important evidence to understand the long-term deformation history, being the only tool that provides rotations about vertical axes characterizing crustal blocks along the geological past. Block-rotation patterns documented along relevant strike-slip faults have proven to be effective in imaging crust deformation of several continental domains of Earth (Kimura et al., 2004, 2011; McKenzie & Jackson, 1986; Piper et al., 1997; Randall et al., 2011; Sonder et al., 1994; Taymaz et al., 2007). On the contrary, little is known

on the internal deformation pattern of strike-slip-bounded crust slivers developed at oblique subduction boundaries, such as those of Ecuador and Peru (Nocquet et al., 2014) and Sumatra (Fitch, 1972; Katili, 1970).

The Chiloé block, located in the southern Andes at 38–48°S latitudes (Figure 1), is a recognized example of a fore-arc sliver undergoing independent motion with respect to nearby plates. It is bounded to the west by the subduction trench between the Nazca and South American plates, to the east by the LOFZ, and it is internally dissected by transverse NW-SE sinistral strike-slip faults (Lange et al., 2008). The LOFZ is a long-living approximately N-S trending dextral strike-slip fault system that runs throughout the volcanic arc of southern Chile and has been active since late Cretaceous times (e.g., Cembrano, Herv, et al., 1996). It extends from the Golfo de Peñas (~47°S) to the Copahue volcano (~38°S) where it is somehow connected to the NE trending transpressional Antiñir-Copahue fault zone, in turn becoming the east verging accretionary front of the Andes (Folguera et al., 2004). First, studies combined field survey and paleomagnetic data to constrain LOFZ and Chiloé block tectonics (Garcia et al., 1988; Cembrano et al., 1992; Beck, 1988, 1991; Beck et al., 2000; Rojas et al., 1994). Subsequently, Hernández-Moreno et al. (2014, 2016) provided a wealth of new paleomagnetic data and largely revised the previous studies, highlighting the complexity of the fore-arc/ arc tectonic system. For instance, the fore-arc sliver is characterized by ubiquitous counterclockwise (CCW) rotations with respect to South America, whereas the LOFZ deformation zone displays >90° clockwise (CW) rotations and diffuse upper crust fragmentation. However, the interaction between the LOFZ and the sinistral transverse faults crosscutting the sliver, LOFZ deformation at northern sliver end, and the relation of this tectonic system with the regional Andean system to the north (Figure 1) is still speculative.

In this study, we present an extensive paleomagnetic study (48 new sites) of the northern termination of the LOFZ and of the Biobio fault (BBF), seemingly the northernmost transverse fault of the Chiloé sliver (Figure 1). Here, the geological bedrock is frequently masked by Plio-Pleistocene glacial deposits (Melnick & Echtler, 2006; Lear et al., 2000), widespread vegetation cover, and—along the LOFZ—by closely spaced stratovolcanoes and related deposits. We combine paleomagnetic data and field and structural evidence in a tectonic model accounting for both the dextral LOFZ and sinistral fault kinematics, and we speculate on the possible reason for the change of Andean deformation style occurring at 38°S.

2. Regional Tectonic Framework

The southern Chile subduction zone is among the most active plate boundaries on Earth, where the largest earthquake ever recorded instrumentally occurred in 1969 (M_w 9.6 Valdivia earthquake, Plafker & Savage, 1970; Figure 1). Here the Nazca plate subducts below South America at a 7–9 cm/year rate (Pardo-Casas & Molnar, 1987; Angermann et al., 1999; Kendrick et al., 2003), but the relative plate movements changed in both direction and rate through the Cenozoic (Pardo-Casas & Molnar, 1987; Quinteros & Sobolev, 2013; Somoza, 1998). From ~50 Ma, the Farallon plate subducted below South America at a ~7 cm/year rate, being characterized by an ~60° angle between convergence direction and trench (also defined 30° subduction obliquity, Somoza, 1998). Between 26 and 20 Ma, obliquity turned to nearly zero as a consequence of the breakup of the Farallon plate into the Nazca and the Cocos plates (Lonsdale, 2005). During this time window, the convergence rate peaked at ~15 cm/year, contemporaneously with the onset of a major deformation phase along the Andean chain (Sempere et al., 1990; Somoza, 1998). From 20 Ma the convergence rate and obliquity decreased to the present-day values, 7–9 cm/year and 15°, respectively (Somoza, 1998). In addition, the Chile Rise—the spreading ridge separating the Nazca and Antarctica plates—began to collide with South America, giving place to the Chile triple junction between the Antarctica, Nazca, and South American plates (Figure 1). The ongoing spreading ridge subduction caused northward triple junction migration trough time up to the current ~46°S latitude (Murdie et al., 1993).

The Chilean Andes between ~38°S and ~46°S are characterized by several tectonic zones distributed subparallel to the trench. In detail, moving eastward from the trench, the following domains are observed (domains 1 to 3 form the fore-arc sliver): (1) the Coastal Platform, made by uplifted Cenozoic marine and coastal sequences; (2) the Coastal Range, constituted by a Permo-Triassic accretionary complex and a late Paleozoic magmatic arc; (3) the Central Depression, a low-relief zone formed by Oligo-Miocene sedimentary and volcanic rocks covered by Plio-Quaternary fluvio-glacial sediments, which tapers out north of 33°S and south of 46°S; (4) the Main Cordillera, composed by Meso-Cenozoic arc-related intrusives (e.g., Patagonian Batholite) and Oligocene-to-present effusive rocks, along with intra-arc continental volcano-sedimentary
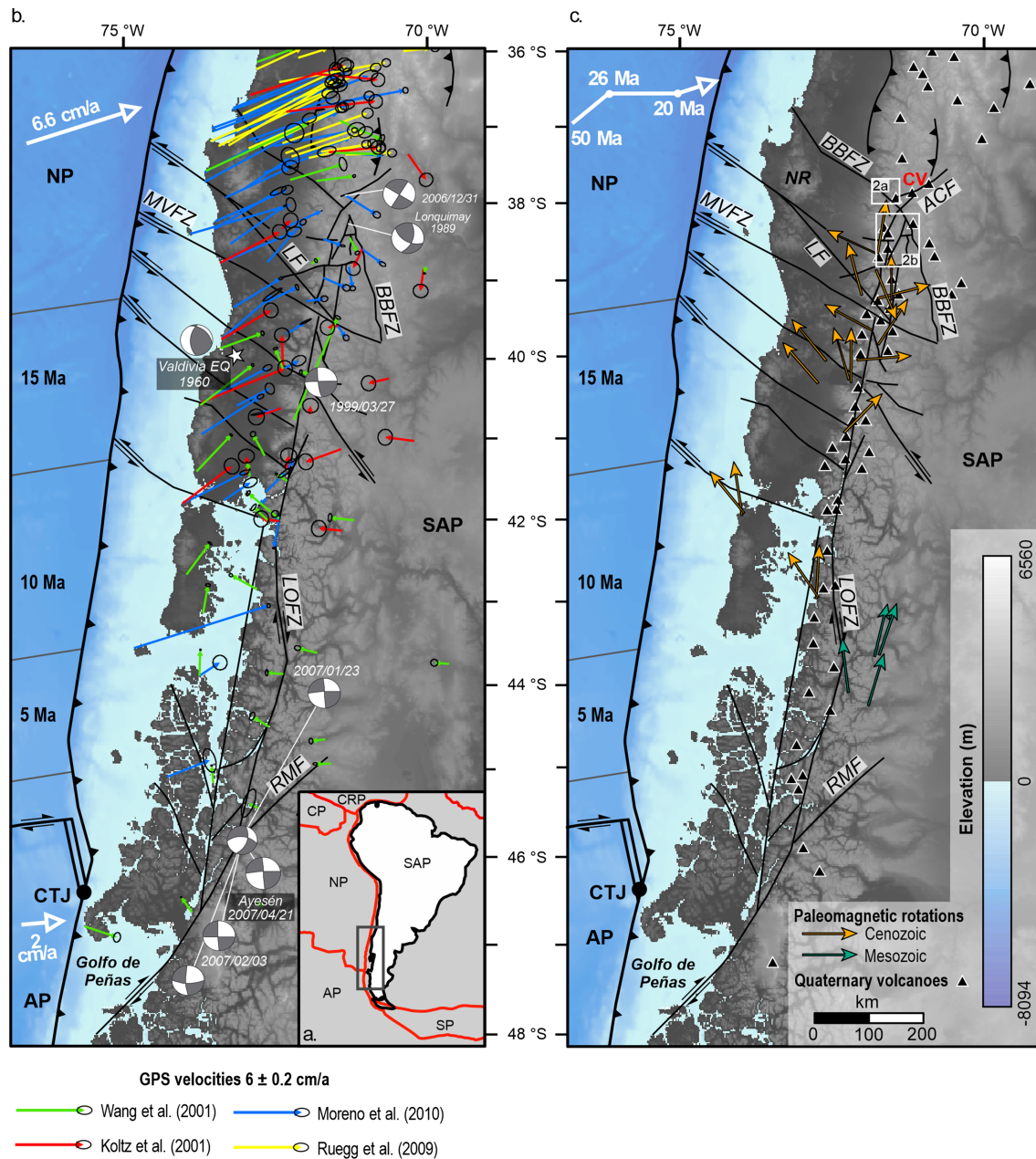
Figure 1. Tectonic setting of the southern Chile subduction zone. (a) Schematic plates assemblage involving the South American Plate (SAP), the Nazca Plate (NP), and the Antarctic Plate (AP), Scotia, Cocos, and Caribbean plates are shown for reference (SP, CP, and CRP, respectively). The dark gray rectangle shows the location of panels b and c. (b) GPS horizontal vector (Wang et al., 2007, Klotz et al., 2001, Moreno et al., 2011, Ruegg et al., 2009) and focal mechanisms (Barrientos & Acevedo-Aránguiz, 1992; Chinn & Isacks, 1983; Dziewonski et al., 1991) highlight the active state of the LOFZ. White bold arrows show the present-day convergence vectors of Nazca and Antarctic plates, with respect to fixed South America (Angermann et al., 1999; Kendrick et al., 2003). (c) Selected paleomagnetic rotations with respect to South America from previous work (Garcia et al., 1988; Cembrano et al., 1992; Rojas et al., 1994; Beck, 1988, 1991; Beck et al., 2000; Hernández-Moreno et al., 2014, 2016). The bold white arrow marks the relative convergence vector of Farralon-Nazca and South American plates in the geologic past (Pardo-Casas & Molnar, 1987; Quinteros & Sobolev, 2013; Somoza, 1998). NR = Nahuelbuta Range; CV = Copahue Volcano; BBFZ = Bio Bio Fault Zone; LF = Lanalhue Fault; ANCF = Antiñir-Copahue Fault; MVFZ = Mocha-Villarica Fault Zone; RMF = Rio Mañiahuales Fault. Main faults are after Hackney et al. (2006).

basins surrounding the LOFZ. North of 38°S, the Main Cordillera is associated with a continuous east verging frontal thrust and a foreland basin system exposed along Andean foothills. Conversely, south of 38°S the active deformation is limited to the intra-arc region and the LOFZ. Such along-strike changes are

also reflected in mean chain elevation that reaches >2.5 km north of 38°S, whereas south of it mean elevation is only ~1 km, the highest peaks being represented by volcanoes.

Chain elevation changes are most likely due to different degrees of strain partitioning. Present-day seismicity and long-term coastal uplift south of 38°S imply an active margin where pure dip-slip convergence occurs at the Chilean trench and in the accretionary wedge (Chinn & Isacks, 1983; Cifuentes, 1989; Barrientos & Acevedo-Aránguiz, 1992; Dewey & Lamb, 1992; Murdie, 1994; Bohm et al., 2002; Lange et al., 2008; Melnick et al., 2006, 2009; Figure 1b). Both the long-term dextral oblique convergence from at least 50 Ma (Cembrano & Hervé, 1993; Hervé, 1976) and the collision of the Chile Rise after 10 Ma could be responsible for strain partitioning in the overriding plate (Cembrano et al., 2000, 2002; Forsythe & Nelson, 1985; Lavenu & Cembrano, 1999; Murdie et al., 1993; Nelson et al., 1993). Although GPS vectors are strongly influenced by postseismic deformation related to viscous stress relaxation in the mantle after the Valdivia earthquake (inland and coastal sites show opposites motions, Khazaradze et al., 2002; Hu et al., 2004; Wang et al., 2007), they reveal a 6.5 mm/year northward Chiloé sliver motion (Klotz et al., 2001; Wang et al., 2007; Ruegg et al., 2009; Moreno et al., 2011; Figure 1b). The northward Chiloé block motion seems to decrease north of 38°S, finally ending at ~33°S where the thickened central Andean crust and the flat-slab subduction together with the consequent lack of volcanism preclude strain partitioning at the crustal scale (Rosenau et al., 2006; Siame et al., 2005).

The nature of the NW-SE trending left-lateral faults that cut the Chiloé fore-arc sliver every ~20–40 km from ~37°S (BBF) to 42°S is controversial. Some works considered them as Permo-Triassic basement structures (Glodny et al., 2008), which would cross the LOFZ and extend to the Argentina foreland (Lange et al., 2008), subsequently reactivated with a reverse component and accommodating internal fore-arc deformation (Melnick et al., 2009), as in the Nahuelbuta Range case. On the other hand, Rosenau et al. (2006) proposed a tectonic model accounting for a genetic relation between the LOFZ and the sinistral strike-slip faults west of it, arranged in an SC geometric relation. Strike-slip crustal seismicity with focal mechanisms consistent with transversal fault orientation and kinematics—thus testifying the active nature of the left-lateral faults—was documented (Bohm et al., 2002; Haberland et al., 2006; Lange et al., 2008; Sielfeld et al., 2019).

3. The Biobio and LOFZ

The BBF is apparently the northernmost of the NW-SE sinistral strike-slip faults crosscutting the fore-arc sliver (e.g., Hackney et al., 2006). It cuts the upper plate from the Pacific coast to the Main Cordillera, presumably crossing the LOFZ (Hackney et al., 2006; Bohm et al., 2002; Rosenau et al., 2006) and following the Biobio valley with a NNW-SSE trend (Figure 2). Little of its deformation history is known from the literature. It is generally considered a Paleozoic first-order discontinuity (Rapela & Pankhurst, 1992; Bohm et al., 2002) that separated fore-arc segments with different metamorphic and magmatic histories during pre-Andean orogeny (Hackney et al., 2006; Glodny et al., 2008). Shallow seismicity highlighted by temporary seismic arrays seems to show that the western BBF segment, where it enters into the Coastal Cordillera, is active (Bohm et al., 2002).

The LOFZ is a ~1,000 km long NNE-SSW right-lateral fault system that runs from 47°S, just south of the Chile triple junction, to the Copahue volcano at ~38°S (Lavenu & Cembrano, 1999; Rosenau et al., 2006; Figure 1c) following the Miocene-Holocene volcanic arc (Cembrano & Lara, 2009). At its southernmost tip, the fault curves to the west following the southern margin of the Golfo de Peñas and ends at sea (Figure 1b). Along its central-northern part, from 42°S to 38°S, longer segments that trend NNE-SSW are connected in a right-stepping geometry by segments trending NE-SW (Figure 1b). North of the Copahue volcano, the LOFZ continues in the NE trending Antiñir-Copahue fault system that marks the active eastern orogenic front of the Andes between 38°S and 37°S (Folguera et al., 2004).

The deformation history of the LOFZ is partially constrained with absolute and relative dating methods. For instance, undeformed dykes crosscutting mylonitic belts along the fault trace yielded contrasting ages of 29 ± 1, 48, and 100 ± 2 Ma, using K/Ar on the bulk rock composition, Ar/Ar dating on biotite grains, and Ar/Ar on hornblende grains, respectively (Cembrano et al., 2000; Hervé, 1976; Schermer et al., 1996). The likely most reliable Ar/Ar ages constrain LOFZ onset to a mid-Cretaceous-early Cenozoic time window, suggesting that it represents a remarkably old tectonic feature of the southern Andes. Early Cretaceous sinistral displacement has been deduced by microstructural analysis at the northernmost fault portion (Cembrano
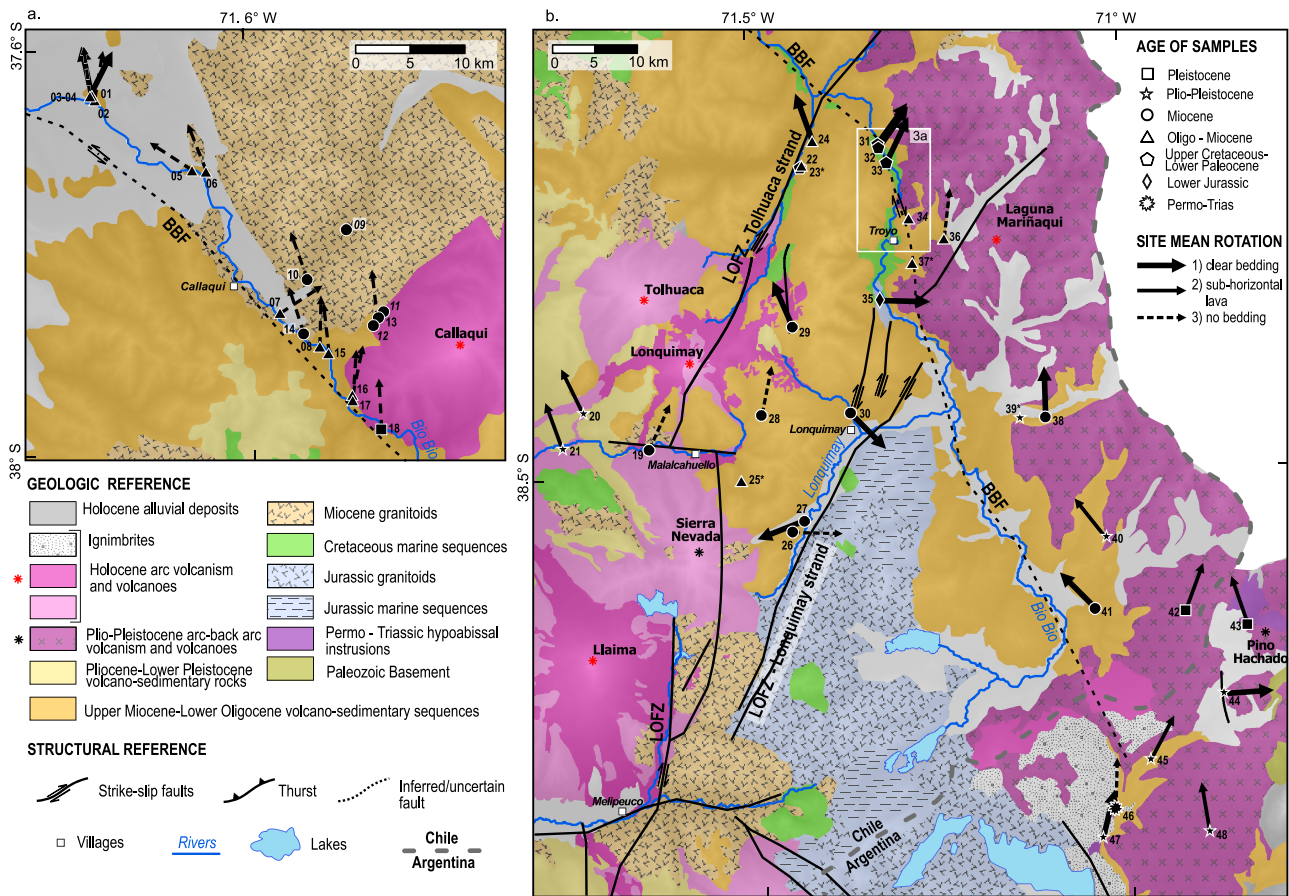
Figure 2. Geologic background along the BBF and northern LOFZ termination, together with paleomagnetic rotations with respect to South America from this work. Main faults are after Hackney et al. (2006), and geology is after Suárez and Emparan (1997) and SERNAGEOMIN, 2003. Sampling sites are identified by their lab number and with a symbol corresponding to the mean age of sampled rocks. The number of failed and rejected sites are given in italics and followed by an asterisk, respectively. Rotation arrows are classified considering bedding evidence from the sampling site. Solid thick arrows are for sites where bedding was clear (class 1); solid thin arrows are for subhorizontal lava (class 2); dashed arrows are for sites where bedding was not clear (class 3). (a) Western BBF portion. (b) Eastern BBF and northern LOFZ end.

et al., 2000). The LOFZ acted as a dextral strike-slip fault during the initial right-oblique subduction episodes between 50 and 26 Ma (Hervé, 1994; Cembrano, Schermer, et al., 1996; Pardo-Casas & Molnar, 1987).

Geochronologic and thermochronologic dating of the ductile-deformed rocks between 46°S and 43°S revealed a Mio-Pliocene activity of right-lateral transpressional shear zones defining a regional transpressional pop-up (Cembrano et al., 2002). Exhumation onset at 16–10 Ma with increasing rates between 7 and 2 Ma—contemporaneously with the Chile Rise collision that induced a late Cenozoic transpression at the southern LOFZ end (Cembrano et al., 2002; Thomson, 2002; Adriasola et al., 2006; Melnick et al., 2009)—would explain the most recent dextral motion along the LOFZ (Cembrano et al., 2000; Lavenu & Cembrano, 1999). Conversely, the lack of significant exhumation documented before 16 Ma suggests a pure strike-slip or transtensional movement (Thomson, 2002). Finally, an alternation of strike-slip and transpressional phases during the Plio-Quaternary was inferred by structural data gathered along the entire fault trace (Lavenu & Cembrano, 1999).

The total horizontal offset along the LOFZ is unknown due to the lack of easily identifiable geologic markers. A post-Triassic 120 km dextral displacement was proposed considering the offset of a Late Paleozoic transverse fault (Gastre fault; Rapela & Pankhurst, 1992), whereas a 30 km Cenozoic displacement was inferred by the offset of a plutonic body (Adriasola et al., 2006). Maximum 124 km and minimum 67 km offset values were hypothesized relying on structural analysis data by Rosenau et al. (2006) at the southern and northern LOFZ end, respectively, with a corresponding northward decrease of Pliocene-to-present slip rates from 32 ±

6 to 13 ± 3 mm/year. Finally, Hernández-Moreno et al. (2014) paleomagnetically calculated a 120 km post-5 Ma horizontal displacement, using the relation between fault offset, maximum paleomagnetic rotation values, and width of the block-rotation zone proposed by Lamb (1987).

Present-day northward movement of the Chiloé block recorded by GPS data implies a 6.5 mm/year LOFZ slip rate that tapers to null values at the northern 37°S fault termination (Klotz et al., 2001; Wang et al., 2007; Ruegg et al., 2009; Moreno et al., 2011; Figure 1b).

Few and shallow (depth <30 km) earthquakes, clustered at the northern and southern LOFZ tips, demonstrate an ongoing right-lateral shear (Chinn & Isacks, 1983; Dziewonski et al., 1991; Barrientos & Acevedo-Aránguiz, 1992; Nelson et al., 1993; López-Escobar et al., 1995; Lavenu & Cembrano, 1999; Lara et al., 2004; Melnick et al., 2006; Lange et al., 2008; Cembrano & Lara, 2009). The irregular seismicity distribution has been related to variable plate coupling at the subduction interface, which would be higher along the central LOFZ portion and lower at its tips (Hackney et al., 2006). Temporary seismic array also reveals a compartmentalization of seismic behavior along the LOFZ, showing a progressive transition from fully localized to splay faulting moving northward along the fault trace (Sielfeld et al., 2019).

4. Paleomagnetic Background

A synthesis of the paleomagnetic rotation pattern documented by previous studies is shown in Figure 1c, where selected data from Garcia et al. (1988), Cembrano et al. (1992), Rojas et al. (1994), Beck, 1988; Beck, 1991; Beck et al., 2000), and Hernández-Moreno et al. (2014, 2016) are reported. Rotation values relative to data published before the year 2014 are according to Hernández-Moreno et al. (2014), who recalculated rotations using updated South America reference poles by Torsvik et al. (2008).

Previous paleomagnetic data, along and across the LOFZ, reveal a complex pattern that has been widely reviewed by Hernández-Moreno et al. (2014). The forearc is characterized by a largely predominant CCW rotation pattern, where rotations up to 170° are observed over distances >100 km from the LOFZ. Conversely, pervasive crustal fragmentation is documented adjacent to the LOFZ, where CW rotations up to 170° are observed east of the fault and constrain blocks (both equidimensional and elongated crust slivers) in the 1–10 km range. Hernández-Moreno et al. (2014) showed that to the east of the LOFZ and at 38–40°S latitudes, CW rotations reach values of 150–170° and rapidly fade out at only 10 km from the fault trace (Figure 1c). The rotation age is constrained to the post-mid-Cenozoic (Beck et al., 2000; Hernández-Moreno et al., 2014).

Different tectonic models have been proposed to explain the paleomagnetic rotation pattern along the LOFZ and in the fore-arc sliver. Beck et al. (1993) suggested that the northward motion of the fore-arc sliver is hampered by the thickened central Andes crust ("buttress effect"). As a consequence, the forearc would break with conjugate-to-the-LOFZ faults forming lens-shaped blocks that rotate CCW. Such model would explain CW rotations occurring within and east of the LOFZ and the concomitance of extensional and compressional deformation along the LOFZ but requires dextral kinematics for the NW-SE transverse faults cutting the forearc, while geological and seismological evidence clearly shows their sinistral nature. Rosenau et al. (2006) considered the LOFZ and the NW-SE transverse faults as a conjugate set of SC structures, forming sigmoidal and poorly deformed blocks. Hernández-Moreno et al. (2014, 2016) suggested that the paleomagnetic rotation pattern along the LOFZ can be explained by a quasi-continuous crust deformation model (McKenzie & Jackson, 1983; Nelson & Jones, 1987; Sonder et al., 1994). In addition, high-resolution paleomagnetic sampling near the LOFZ showed that the upper crust is fragmented into 1–10 km wide rigid blocks and elongated slivers, at odds with the continuous deformation model proposed by Rosenau et al. (2006). In this context, the regional CCW pattern in the fore-arc region would be due to quasi-continuous crust deformation related to the sinistral activity of the NW-SE faults (Hernández-Moreno et al., 2014, 2016; Lange et al., 2008).

5. Field Evidence From the BBF and the Northern LOFZ Segment

We investigated in the field the area comprised between the Callaqui and the Llaima volcanoes, following the traces of the BBF and the LOFZ, the two major strike-slip faults exposed there (Figure 2).

The BBF was investigated in the fore-arc (western segment, between 71.8°W and 71.5°W; Figure 2a) and intra-arc regions (eastern portion, between 71.2°W and 71.1°W; Figure 2b). Holocene deposits of both
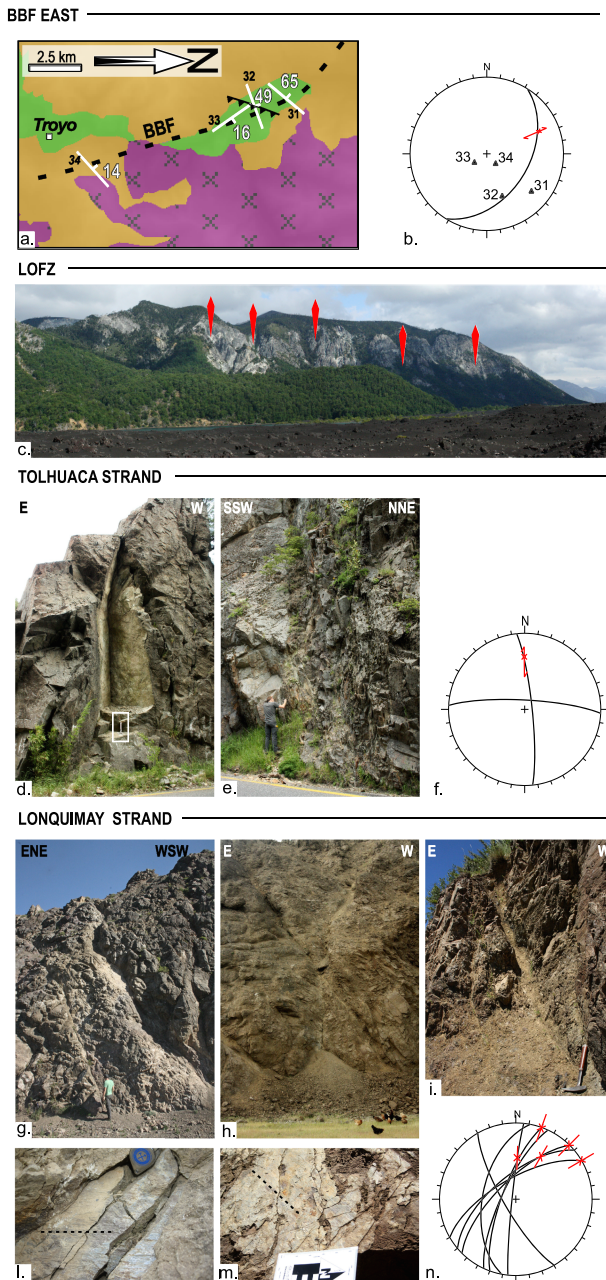
Figure 3. Field observations and structural measurement along the BBF and LOFZ. In the equal-area projection plots, black solid lines mark fault planes, and red arrows indicate measured senses of shear. Black triangles are pole to bedding. (a) Zoomed map of the eastern BBF in the Troyo area (north to the right; see location in Figure 2b). At sampling Site 32, a thrust fault accommodating oblique dextral displacement has been measured. (b) Measured bedding following the supposed BBF trace (BBF) show increasing dip toward the north. (c) Field picture of the LOFZ east of the Llaima volcano. (d) Tolhuaca strand cutting through Miocene intrusive. Hammer highlighted in the white box is for scale. (e) Transverse deformation band cutting the Tolhuaca strand at sampling site BBF19 (Figure 2b). (f) Stereonet of structures measured along the Tolhuaca strand. (g, h) Damage zones of the Lonquimay strand at sampling sites BBF27, 30, and 35 respectively. (l, m) Slickenlines measured on fault planes in panels h and i, respectively. (n) Fault data collected along the Lonquimay strand highlight both dip-slip and strike-slip shear along subvertical planes.

alluvial and volcanic origin largely hide the bedrock all along the BBF (SERNAGEOMIN, 2003; Suárez & Emparan, 1995). Along its western portion, Oligo-Miocene intra-arc volcano-sedimentary sequences and Miocene granitoids of the Northern Patagonian Batholite crop out in isolated spots (Figure 2a). Strikingly, neither localized nor diffuse deformation was recognized, and fault planes or any related deformation attributable to the BBF were not observed. Similarly, along the BBF eastern portion, after that it crosses the LOFZ and slightly changes its strike (Figure 2b; Suárez & Emparan, 1995; Bohm et al., 2002), no evidence of sinistral strike-slip faulting is apparent. Conversely, close to paleomagnetic site BBF32, we observed a 44° SE dipping fault (i.e., subparallel to the mean LOFZ trend) showing reverse and dextral displacement indicators (Figures 3a and 3b). Bedding measured in surrounding outcrops yields on average the same trend and shows an increase of dip values moving northward (Figures 3a and 3b).

North of the Llaima volcano, where the LOFZ trends N-S and juxtaposes Miocene granitoids and lava flows from the Llaima volcano (Hernández-Moreno et al., 2014; Figures 2b and 3c), the northern LOFZ termination is composed by at least two major stepping eastward strands and by minor deformation bands (Suárez & Emparan, 1995).

We refer to the Tolhuaca strand as the western fault segment located adjacent to the Lonquimay and Tolhuaca volcanoes and to the Lonquimay strand as the eastern segment that runs near the Lonquimay village and follows the namesake river (Figure 2b). Along the Tolhuaca strand, close to the paleomagnetic site BBF19 (Figure 2b), we observed a N-S subvertical fault with dextral transtensive indicators cutting into intrusive rocks (Figures 3d, 3f, and supporting information Table S1). Here we also observed a sinistral shear along a W-E deformation bend composed by a succession of near-vertical and poorly spaced anastomosed planes (Figure 3e). East of the Tolhuaca strand, the NNE-SSW Lonquimay strand (Figure 2b) cuts through Miocene granitoids and Jurassic volcano-sedimentary succession of the Neuquén basin (Suárez & Emparan, 1995; SERNAGEOMIN, 2005), strongly influencing the landscape as the Lonquimay River and valley follow it (Figure 2b). Although the fault trace is rarely observable in the field (it is often covered by Holocene alluvial deposits, Suárez & Emparan, 1995), when apparent the deformation is much more intense than that observed along the Tolhuaca strand. Pervasively deformed outcrops occur, as observed at sites BBF27, 30, and 35 (Figure 2b). Here the Oligo-Miocene continental and Jurassic-Cretaceous marine sediments are intensely faulted and fractured (Figures 3g–3n). We observed high-angle faults with fault gouges between 5 and 10 cm wide and tens of meters wide damage zones (Figures 3g–3i). N-S to NE-SW faults planes with purely strike-slip (Figure 3l) and oblique slickenlines (Figure 3m) are preserved in the host rock (Figure 2b). At site BBF35, located at the northern end of the Lonquimay strand, NNE-SSW subparallel and smaller faults were observed (Figure 2b). Here, slickenlines (Table S1) indicate oblique displacement (Figure 3m) but no offset was detectable. To the north, the Lonquimay strand is reported to end at the junction with the BBF trace (Figure 2b; Suárez & Emparan, 1995), although no evidence was found for that in the field.

The back-arc region, east of 71.2°W, is characterized by the widespread exposure of Plio-Pleistocene arc and back-arc-related lavas and subordinate ignimbrites that unconformably overly an Oligo-Miocene

continental succession (Zanettini et al., 2010). In the Pino Hachado zone, Plio-Pleistocene lavas and small and scattered outcrops of Paleozoic and Permo-Triassic basement rocks without apparent deformation occur (Zanettini et al., 2010).

6. Paleomagnetic Sampling and Methods

We collected 368 paleomagnetic samples at 48 sites, of which 330 gave valuable results (Figure 2 and Table 1). At each site we drilled 5–10 cores (7 on average) by means of a petrol-powered portable drill cooled by water and oriented them in situ using the Sun (when possible) and a magnetic compass, corrected for the local geomagnetic declination in February 2015 (between 6°E and 8°E according to NOAA's National Geophysical Data Center, http://www.ngdc.noaa.gov/geomag/declination.html).

We preferentially collected lavas and ignimbrites, mostly Oligo-Miocene in age and few (four sites) intrusive rocks. We avoided sampling historic or Holocene lavas from active volcanoes, as they are unlikely to have accumulated significant tectonic rotations after emplacement. Each site gathered in volcanic rocks was sampled within an individual unit that presumably records a "snapshot" of the local geomagnetic field direction occurring at the eruption time. Therefore, at the individual site level the paleo secular variation (PSV) of the geomagnetic field is surely not averaged out, as it would need in paleomagnetic studies aimed at tectonic reconstructions. We will explain below how we deal with such directional scatter source. Furthermore, as wrong bed tilt estimates translate to wrong paleomagnetic rotation values, we identify three different classes of bedding that imply different reliability of paleomagnetic data. Besides best sites with clear bedding (Class 1) and sites with no bedding apparent (Class 3) sites sampled in subhorizontal lavas are considered of reasonably fair quality (Class 2), as tilting is assumed to have been not significant.

The cores were successively cut into standard paleomagnetic specimens of 22 mm height, and paleomagnetic measurements were performed in the shielded room of the Istituto Nazionale di Geofisica e Vulcanologia (INGV, Roma), by means of a 2G Enterprises direct current-superconducting quantum interference device cryogenic magnetometer. Alternating field (AF) yielded by three coils online with the magnetometer until a maximum AF peak of 120 mT was routinely used in 11 steps to demagnetize samples. Thirty-seven samples from 14 sites that were not demagnetized at 120 mT and one specimen from each site were thermally cleaned using a Pyrox shielded oven in 10 steps up to 640 °C.

Demagnetization data were plotted on orthogonal vector component diagrams (Zijderveld, 1967), and principal component analysis was used to identify magnetization components (Kirschvink, 1980). Site-mean paleomagnetic directions were computed using Fisher's (1953) statistics and plotted on equal-angle projections. Paleomagnetic rotation and flattening values with respect to stable South America were calculated according to Demarest (1983), using reference paleopoles from Torsvik et al. (2012). Mean ages of the sampled rocks as derived from absolute and/or relative dating from available geological maps were used to select the corresponding age paleopole. The rotation sense was defined with the conservative approach that considers the smaller angle between the observed and expected declinations, thereby calculating rotation values always ≤|180°|. In addition, hysteresis properties of one sample per site have been measured. Method and results are reported in the supporting information.

Our sampling strategy aimed at characterizing the fore-arc sliver deformation in the frame of the Andean chain; thus, samples were collected in the fore-arc, arc, back-arc regions and following and crossing both BBF and LOFZ faults traces (Figure 2).

Eighteen sites were collected at both sides and at a <10 km distance, from the BBF western portion, between 71°50′W and 71°32′W (Figures 1 and 2a). Of these, 11 sites were taken from lava layers interbedded in the Oligo-Miocene Cura Mallín continental succession (Om2c in Table 1) that is constrained by K-Ar dating between 22.0 ± 0.9 and 11.0 ± 1.6 Ma (Suárez & Emparan, 1997). Two sites were sampled in Miocene granitoids of the Northern Patagonian Batholite, whose age is constrained by K-Ar dating on biotite minerals between 15.2 ± 1.2 and 7.2 ± 1.9 Ma (Suárez & Emparan, 1997). Four sites were sampled in Miocene lava remnants of volcanic edifices (M3i in Table 1; SERNAGEOMIN, 2003), and one site was collected in Pleistocene basaltic lavas (SERNAGEOMIN, 2003). Only 2 out of 18 sites displayed clear bedding (Figure 2a).

Further east, we sampled five sites along the BBF eastern portion in the vicinity of the Troyo village, after that it crosses the LOFZ and changes strike (Figure 2b). Of these, three sites with clear bedding (BBF31-

Table 1
Paleomagnetic Site Mean Directions From the Biobio and Liquiñe-Ofqui Fault Zones

Site	Unit map	Unit name	Lithology	Latitude S	Longitude W	Age	Age (Ma)	Bedding (dirdip/dip)	D (deg)	I (deg)
				Geographic coordinates					ChRM component In situ	
BBF01	Om2c	Lavas de Huelehueico	Basaltic Lava	37°42′ 37.7640″	71°49′ 18.7320″	Late Oligocene-Early Miocene	20 ± 1	—	7.3	−43.8
BBF02	Om2c	Cura Mallín	Basaltic Lava	37°42′ 23.1840″	71°49′ 28.6680″	Late Oligocene-Early Miocene	28–18.8	292/12	335	−45
BBF03	Om2c	Cura Mallín	Dike Intruding siteBBF04	37°42′ 24.8400″	71°49′ 36.1560″	Late Oligocene-Early Miocene	28–18.8	—	170.2	47
BBF04	Om2c	Cura Mallín	Ignimbrite	37°42′ 24.8400″	71°49′ 36.1560″	Late Oligocene-Early Miocene	28–18.8	292/12	204.2	52.5
BBF05	Om2c	Cura Mallín	Basaltic Lava	37°46′ 13.1160″	71°43′ 22.4040″	Late Oligocene-Early Miocene	28–18.8	—	120.4	71.5
BBF06		Cura Mallín	Basaltic Lava	37°46′ 18.0840″	71°42′ 31.8600″	Late Oligocene-Early Miocene	28–18.8	—	156.2	58.9
BBF07	Om2c	Cura Mallín	Basaltic Lava	37°53′ 22.1280″	71°38′ 10.0320″	Late Oligocene-Early Miocene	28–18.8	—	54.3	−35.8
BBF08	Om2c	Cura Mallín	Basaltic Lava	37°55′ 5.7000″	71°35′ 44.7360″	Late Oligocene-Early Miocene	28–18.8	—	358.9	−49.1
BBF09	Mg	North Patagonia Batholite	Dike intruding granodiorite	37°49′ 22.4760″	71°33′ 52.8120″	Miocene	18–6	—	—	—
BBF10	Mg	North Patagonia Batholite	Dike intruding granodiorite	37°51′ 46.1520″	71°36′ 24.4080″	Miocene	18–6	—	158.4	60.7
BBF11	M3i	M3i	Basaltic Lava	37°53′ 27.8160″	71°31′ 42.4920″	Early -Middle Miocene	23–14	—	—	—
BBF12	M3i	M3i	Basaltic Lava	37°53′ 44.2320″	71°32′ 3.4440″	Early -Middle Miocene	23–14	—	—	—
BBF13	M3i	M3i	Acidic lava	37°54′ 7.9560″	71°32′ 22.6320″	Early -Middle Miocene	23–14	—	351.2	−25.3
BBF14	M3i	M3i	Basaltic Lava	37°54′ 26.1360″	71°36′ 44.3160″	Early -Middle Miocene	23–14	—	340.4	−57.7
BBF15	Om2c	Cura Mallín	Basaltic Lava	37°55′ 26.5080″	71°35′ 13.3080″	Late Oligocene-Early Miocene	28–18.8	—	351	−65.8
BBF16	Om2c	Cura Mallín	Basaltic Lava	37°57′ 30.7800″	71°33′ 48.5280″	Late Oligocene-Early Miocene	28–18.8	—	9	−70.4
BBF17	Om2c	Cura Mallín	Basaltic Lava	37°57′ 47.8440″	71°33′ 47.9520″	Late Oligocene-Early Miocene	28–18.8	—	1.5	−37.9
BBF18	Pl3		Basaltic Lava	37°59′ 15.0360″	71°32′ 3.6960″	Pleistocene	2.6–0.012	—	355.2	−49.3
BFF19	Tm	North Patagonia Batholite	Intrusive	38°28′ 10.8840″	71°38′ 39.0480″	Miocene	18–6	—	203.3	54.3
BFF20	Pplim	Malleco	Basaltic Lava	38°25′ 48.4320″	71°43′ 57.3960″	Pliocene-Pleistocene Inferiore	2.6–0.012	Sub_Hzt	152.9	59.2
BFF21	Pplim	Malleco	Basaltic Lava	38°28′ 2.2800″	71°45′ 41.6520″	Pliocene-Pleistocene Inferiore	2.6–0.012	Sub_Hzt	338.8	−75.2
BBF22	Tvc	Complejo Vizcacha Cumillao	Ignimbrite	38°10′ 24.2760″	71°25′ 48.2880″	Upper Cretaceous-Early Tertiary	100.5–23	—	—	—
BBF23[a]	Om2c	Cura Mallin	Basaltic Lava	38°10′ 15.7080″	71°25′ 40.8360″	Late Oligocene-Early Miocene	29–18.8	—	172	−8.3
BBF24	Om2c	Cura Mallin	Basaltic Lava	38°08′ 42.7200″	71°24′ 45.0000″	Late Oligocene-Early Miocene	29–18.8	347/29	343.8	−32
BBF25[a]	Om2c	Cura Mallín	Basaltic Lava	38°30′ 19.4760″	71°31′ 14.5200″	Late Oligocene-Early Miocene	28–18.8	136/21	32.2	−77.6
BBF26	Om2c	Cura Mallín	Basaltic Lava and intruding dike	38°33′ 39.4920″	71°27′ 10.2960″	Late Oligocene-Early Miocene	28–18.8	—	89.5	−30.9
BBF27	Om2c	Cura Mallín	Basaltic Lava	38°32′ 59.8200″	71°26′ 9.8880″	Late Oligocene-Early Miocene	28–18.8	96/56	109.2	−49.2

Table 1 *(continued)*

				Geographic coordinates				ChRM component In situ	
BBF28	Om2c	Cura Mallín	Dike	38°26'9.7080"	71°29'26.5560"	Late Oligocene-Early Miocene	28–18.8	—	3.5	−48.7
BBF29	Om2c	Cura Mallín	Ignimbrite	38°20'34.6920"	71°26'46.4640"	Late Oligocene-Early Miocene	28–18.8	120/13	338.9	−39.1
BBF30	Om2c	Cura Mallín	Basaltic Lava	38°26'8.9880"	71°22'13.4040"	Late Oligocene-Early Miocene	28–18.8	210/17	146.3	−40.6
BBF31	Tvc	Complejo Vizcacha Cumillao	Basaltic Lava	38°08'59.8920"	71°19'29.2440"	Late Cretaceous-Early Paleocene	100.5–23	310/50	326.2	−36.1
BBF32	Tvc	Complejo Vizcacha Cumillao	Basaltic Lava	38°09'13.5360"	71°19'24.8160"	Late Cretaceous-Early Paleocene	100.5–23	340/49	2.5	−16.3
BBF33	Tvc	Complejo Vizcacha Cumillao	Basaltic Lava	38°10'12.3600"	71°18'48.0600"	Late Cretaceous-Early Paleocene	100.5–23	55/16	211.7	56.3
BBF34	Om2c	Cura Mallín	Basaltic Lava	38°13'29.2800"	71°17'58.7040"	Late Oligocene-Early Miocene	28–18.8	—	—	—
BBF35	Jnb (Miembro Icalma)	Formacion Nacientes del Bio Bio	Basaltic Lava	38°18'58.4280"	71°19'36.5160"	Lower Jurassic	190–174	282/21	94.4	−80.1
BBF36	Om2c	Cura Mallin	Ignimbrite	38°15'9.1440"	71°14'17.8800"	Late Oligocene-Early Miocene	28–18.8	—	3.9	−11.2
BBF37[a]	Om2c	Cura Mallín	Basaltic Lava	38°16'40.0800"	71°16'53.7600"	Late Oligocene-Early Miocene	28–18.8	79/33	72.8	−53.4
BBF38	Msm	Mitraquen	Basaltic Lava	38°26'42.9360"	71°06'23.9040"	Upper Miocene	5.3–0.012	90/04	0.9	−49.9
BBF39[a]	PPl3	Cola de Zorro	Ignimbrite	38°26'29.1120"	71°09'13.2840"	Plio-Pleistocene	5.3–0.012	—	127	5.7
BBF40	Ppliv	Conjunto volcanico I	Columnar basaltic lava	38°34'30.3240"	71°01'39.6120"	Lower Pliocene - Lower Pleistocene	5.3–0.012	Sub_Hzt	140.4	33.4
BBF41	Msm	Mitraquen	Piroclastyc flow deposit	38°39'0.9000"	71°02'42.7560"	Upper Miocene	12–5.3	275/28	117.5	34.5
BBF42	Pliv	Conjunto volcanico II	Basaltic Lava	38°39'15.4800"	70°55'21.1800"	Lower Pleistocene	5.3–0.012	Sub_Hzt	198.4	61.6
BBF43	28	Basalto Hueyeltuè	Columnar basaltic lava	38°40'12.7200"	70°50'19.2120"	Lower Pleistocene	2.6–1.8	Sub_Hzt	159.5	69.6
BBF44	25	Basalto Tipili	Basaltic Lava	38°44'38.3280"	70°52'22.0800"	Pliocene	5.3–3.6	319/25	51.3	−57.8
BBF45	25	Basato Tipili	Columnar basaltic lava	38°48'46.7280"	70°58'27.0840"	Pliocene	5.3–3.6	Sub_Hzt	26.9	−52.3
BBF46	3a	Grupo Choiyoi	Hypabissal body	38°51'46.8360"	71°01'23.9160"	Permo-Trias	259–237	—	343	−51
BBF47	25	Basalto Tipili	Columnar basaltic lava	38°53'43.7280"	71°02'28.2480"	Pliocene	5.3–3.6	309/12	184.9	29.8
BBF48	25	Basalto Tipili	Basaltic Lava	38°53'28.1760"	70°53'45.8880"	Pliocene	5.3–3.6	Sub_Hzt	348.8	−59.5

Note. Geologic reference for sites from 1 to 18: Map 1:100,000. Geologic reference for sites from 18 to 48: Map 1:250,000.
[a] ***Rejected sites*** $a_{95} > 25, |80°| > I < |10°|$; [b] ***failed sites.***

33) were taken in a Cretaceous-Paleogene volcanic and volcano-clastic sequence developed in a subaerial and lacustrine environment (Suárez & Emparan, 1997). As more accurate age is not available for the sampled strata, we assumed for them a mean age of 60 Ma (Table 1). The other two sites are from the Oligo-Miocene Cura Mallín continental succession, one with clear bedding (BBF37) and one with no bedding apparent (BBF34; Figure 2b).

In the fore-arc and arc regions, around the Tolhuaca strand of the LOFZ, we sampled one site (BBF22) in the Cretaceous-Paleogene volcanic sequence, five sites (BBF23, 24, 25, 28, and 29) in lava layers interbedded in

Table 1
Paleomagnetic Site Mean Directions From the Biobio and Liquiñe-Ofqui Fault Zones

| | ChRM component | | | | | | | | | | |
| | In situ | | | Tilt corrected | | Vertical axis rotations | | | | | |
Site	k	α95 (deg)	n/N	D (deg)	I (deg)	Considered palepoles age (Torsvik et al., 2012)	R (deg)	ΔR (deg)	F (deg)	ΔF (deg)	Site
BBF01	224.6	5.1	5/10	—	—	20	9.7	6.2	−17.6	4.3	BBF01
BBF02	6.77	21.4	9/10	345.4	−53	20	−12.2	29.2	−8.4	16.8	BBF02
BBF03	35.99	9.4	8/10	—	—	20	−7.4	11.2	−14.4	7.5	BBF03
BBF04	71.65	6.1	9/10	219.2	50.4	20	26.6	8.3	−9.2	5.0	BBF04
BBF05	38.23	11	6/8	—	—	20	−57.2	29.0	10.0	8.7	BBF05
BBF06	28.73	12.7	6/8	—	—	20	−21.4	19.8	−2.6	10.1	BBF06
BBF07	71.07	7.2	7/8	—	—	20	56.7	7.5	−25.8	5.9	BBF07
BBF08	579.22	2.5	7/8	—	—	20	1.3	4.1	−12.5	2.6	BBF08
BBF09	—	—	—	—	—		—	—	—	—	*BBF09*
BBF10	295.81	3.2	8/8	—	—	10	−19.6	5.4	1.1	2.8	BBF10
BBF11	—	—	—	—	—	—	—	—	—	—	*BBF11*
BBF12	—	—	—	—	—	—	—	—	—	—	*BBF12*
BBF13	44.08	9.2	7/8	—	—	20	−6.4	8.4	−36.3	7.4	BBF13
BBF14	54.97	16.8	3/7	—	—	20	−17.2	25.0	−3.9	13.2	BBF14
BBF15	150.38	4.5	8/8	—	—	20	−6.6	9.0	4.2	3.9	BBF15
BBF16	94	6.3	7/8	—	—	20	11.4	15.1	8.7	5.2	BBF16
BBF17	204.87	3.4	10/10	—	—	20	3.9	4.4	−23.8	3.1	BBF17
BBF18	91.14	5.8	8/8	—	—	1	−3.1	7.2	−8.6	4.7	BBF18
BFF19	34.21	9.6	8/10	—	—	20	25.0	13.0	−7.7	7.6	BBF19
BFF20	336.01	3.7	6/8	—	—	1	−25.3	5.9	0.8	3.2	BBF20
BFF21	158.92	4.4	8/8	—	—	1	−19.4	13.7	16.8	3.6	BBF21
BBF22	—	—	—	—	—	—	—	—	—	—	*BBF22*
BBF23[a]	5.14	29.5	7/8	—	—	—	—	—	—	—	**BBF23**[a]
BBF24	93.52	5	10/12	337.1	−60.4	20	−20.5	8.4	−1.4	4.2	BBF24
BBF25[a]	2.62	37.5	10/10	343.7	−63.3	—	—	—	—	—	**BBF25**[a]
BBF26	59.07	6.3	10/10	—	—	20	92.0	6.3	−31.2	5.1	BBF26
BBF27	48.64	8.7	7/10	247.3	−71.9	20	−110.3	22.2	9.2	7	BBF27
BBF28	140.1	4.7	8/8	—	—	20	11.0	6.2	−13.3	4.0	BBF28
BBF29	8.47	20.2	8/9	333.7	−28.6	20	−23.8	18.2	−33.4	15.8	BBF29
BBF30	22.69	11.9	8/9	130.9	−46.1	20	134.7	13.8	−15.9	9.4	BBF30
BBF31	119.36	5.5	7/8	28.2	−76.7	60	35.8	19.3	14.2	4.5	BBF31
BBF32	38.76	8.4	9/10	24.8	−58.6	60	35.4	12.9	−3.9	6.6	BBF32
BBF33	60.04	8.7	6/8	194.8	70.1	60	25.4	20.7	7.6	6.9	BBF33
BBF34	—	—	—	—	—	—	—	—	—	—	*BBF34*
BBF35	52.01	10.7	5/8	99.5	−59.1	180	91.4	17.0	−0.4	8.7	BBF35
BBF36	100.45	4.8	10/11	—	—	20	6.3	4.7	-50.7	4.1	BBF36
BBF37[a]	47.04	7.1	10/10	32	-84.9	—	—	—	—	—	**BBF37**[a]
BBF38	166.74	5.2	6/8	356.2	−49.8	10	−1.7	6.5	−10.3	4.2	BBF38
BBF39[a]	5.76	23.5	9	—	—	—	—	—	—	—	**BBF39**[a]
BBF40	136.99	4.7	8/8	—	—	2	−38.3	4.8	−25.5	3.9	BBF40
BBF41	43.9	9.2	7/8	132.8	59	10	−45.1	14.2	−1.3	7.3	BBF41
BBF42	169.56	4	9/10	—	—	2	20.0	6.8	3.0	3.4	BBF42
BBF43	122.79	5	8/8	—	—	2	−18.5	11.4	11.0	4.1	BBF43
BBF44	231.1	4	7/8	84.3	−49.2	4	86.1	5.1	−9.3	3.3	BBF44
BBF45	24.63	11.4	8/8	—	—	4	28.7	14.8	−6.4	9.0	BBF45
BBF46	311.24	3.1	8/8	—	—	250	1.4	5.6	−14.4	3.2	BBF46
BBF47	401.67	2.8	8/8	191.6	36	4	13.3	3.3	−22.7	2.5	BBF47
BBF48	69.51	9.2	5/8	—	—	4	−9.4	14.5	0.7	7.3	BBF48

AGU
100
ADVANCING EARTH
AND SPACE SCIENCE

Tectonics

10.1029/2019TC005881

the Cura Mallín continental volcano-clastic succession, one site (BBF19) in Miocene intrusives (Suárez & Emparan, 1997) and two sites (BBF20, 21) in Plio-Pleistocene sub-horizontal lavas (Suárez & Emparan, 1997).

Close to the Lonquimay strand, we sampled three sites (BBF26, 27, and 30) in lava layers of the Oligo-Miocene succession and one site (BBF35) in the Lower Jurassic volcanic sequence of the Neuquén back-arc basin (Suárez & Emparan, 1997; Howell et al., 2005). The bedding was clear for three out of four sites (Figure 2b).

Finally, 12 sites were sampled in the back-arc region east of the Lonquimay strand and the BBF. One site (BBF46) was drilled in a Permo-Triassic hypabyssal intrusion (Zanettini et al., 2010), one site (BBF36) in Oligo-Miocene ignimbrites ascribed to the Cura Mallín succession (Suárez & Emparan, 1997), and two sites (BBF38, 41) in a lava and a pyroclastic flow (Table 1) from the Upper Miocene Mitrauquén continental formation. Such unit, exposed only to the east of the Biobio River, is dated at 9.5–8.0 Ma by whole-rock K-Ar technique (Suárez & Emparan, 1997). Eight sites were collected in Plio-Pleistocene ignimbrite (BBF39) and subhorizontal lavas (BBF40, 42–48) dated between 5 and 1 Ma by K-Ar on whole rocks (Suárez & Emparan, 1997). Alkaline and subalkaline lava compositions suggest transitional arc-back-arc affinity (Muñoz & Stern, 1988, 1989).

7. Paleomagnetic Results

Samples from 5 out of 48 sites yielded erratic demagnetization diagrams and were thus excluded from further consideration (Table 1). In the remaining 43 sites, a viscous component was removed at 20 mT or 200 °C (Figure 4), and in few cases, a low coercivity component likely given by lightning effects was isolated between 20 and 40 mT (Figure 4o). A characteristic paleomagnetic component (ChRM) was successively identified in the 20–120 mT and 200–600 °C AF field and temperature intervals, respectively. About 80% of the samples was completely demagnetized at 120 mT or 550–600 °C, indicating low-Ti titano-magnetite as the main magnetic carrier. Samples from 14 sites that still held a significant remanence at 120 mT were thermally cleaned up to 640 °C indicating the occurrence of hematite along with magnetite (Figures 4c, 4h, and 4i).

The α_{95} values relative to the site-mean paleomagnetic directions vary from 2.5° to 37.5° (9.0° on average; Figure 5 and Table 1). Four additional sites were discarded according to the following criteria: (1) α_{95} > 25°, (2) k < 5, and (3) mean inclination value <|10°|or >|80°|(subhorizontal inclinations have undefined magnetic polarity whereas subvertical inclinations imply very large declination uncertainties; the local expected inclination value calculated assuming a geocentric axial dipole field is −58°). After having applied such reliability criteria, 39 site-mean paleomagnetic directions were retained to infer on the tectonic rotation pattern.

Site-mean paleomagnetic directions show both normal (26 sites) and reverse (13 sites) polarity (Figure 5). The limited amount of sites yielding clear bedding represents a limit for performing the reversal and fold test on the paleomagnetic data set. The results of the reversal (McFadden & McElhinny, 1990) and fold tests (McFadden, 1990) performed separately on group of sites from given tectonic domains and on the whole data set are reported in supporting information. The reversal test is positive for the sites located along the western portion of the BBF fault trace and undetermined for those located along the eastern BBF fault trace. The fold test is undetermined considering the entire data set and is negative for the fore-arc group, possibly due to the large declination dispersion and to the low number of available sites, respectively. The entire group of sites located to the W of the LOFZ and the specific intra-arc group (that considers only the data from the Lonquimay strand of the LOFZ) pass the fold test at the 95% and 99% probability, respectively. In any case, the magnetic mineralogy dominated by magnetite, the occurrence of dual magnetic polarities, and the spread of both in situ and tilt corrected paleomagnetic directions that are generally far from the local geocentric axial dipole field direction (Figure 5) suggest a lack of remagnetization phenomena and support the primary nature of the isolated ChRMs. Therefore, the differences between observed and expected South American declinations are inferred to be mostly related to tectonic rotations, although the PSV of the geomagnetic field recorded by sites sampled in volcanic units surely played a role for paleomagnetic direction scatter.
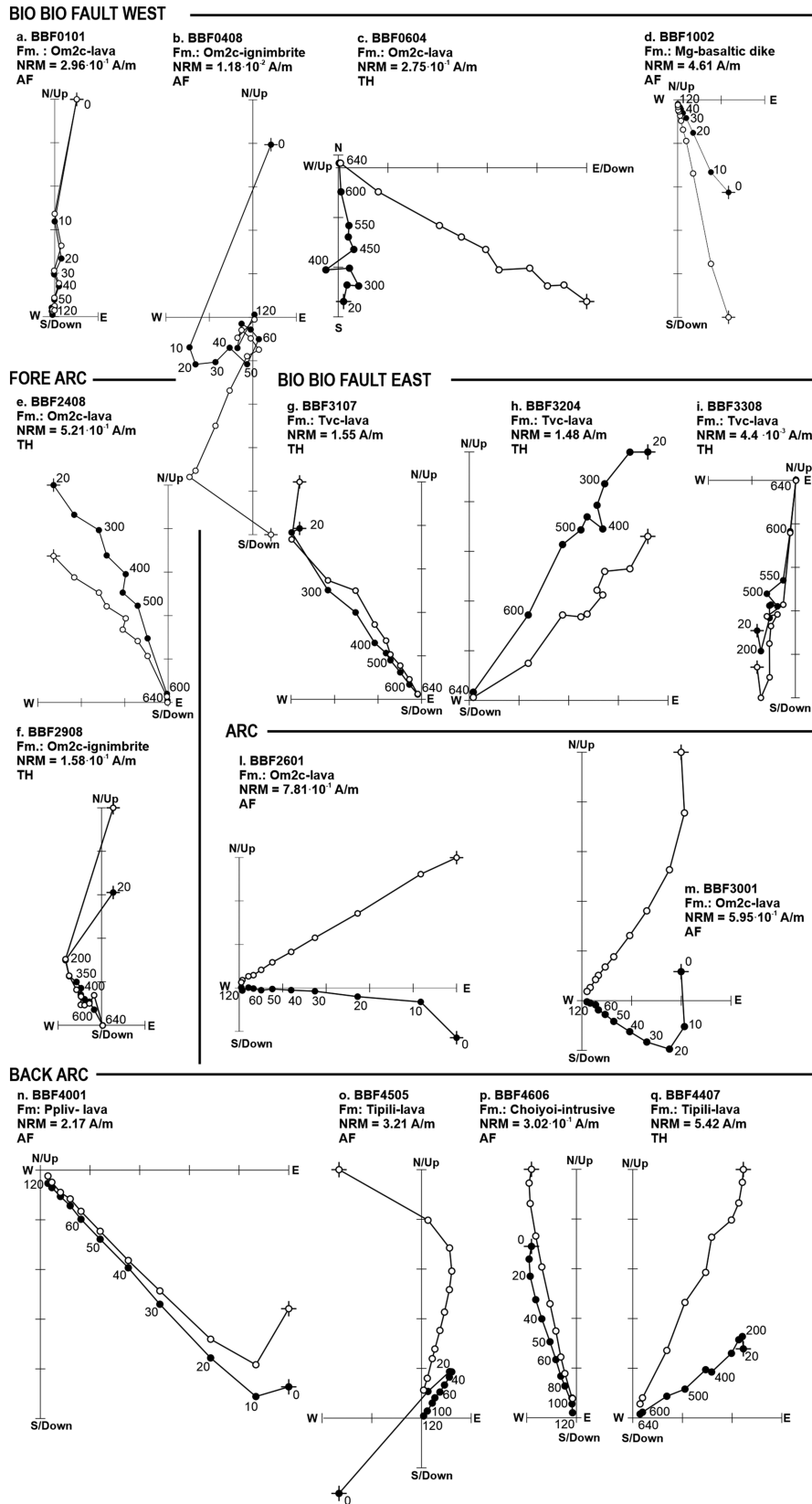
Figure 4. Orthogonal vector diagrams of typical demagnetization data, in in situ coordinates. Solid and open circles represent projection on the horizontal and vertical planes, respectively. Demagnetization steps are in millitesla for alternating field (AF) and in °C for thermal demagnetization (TH).
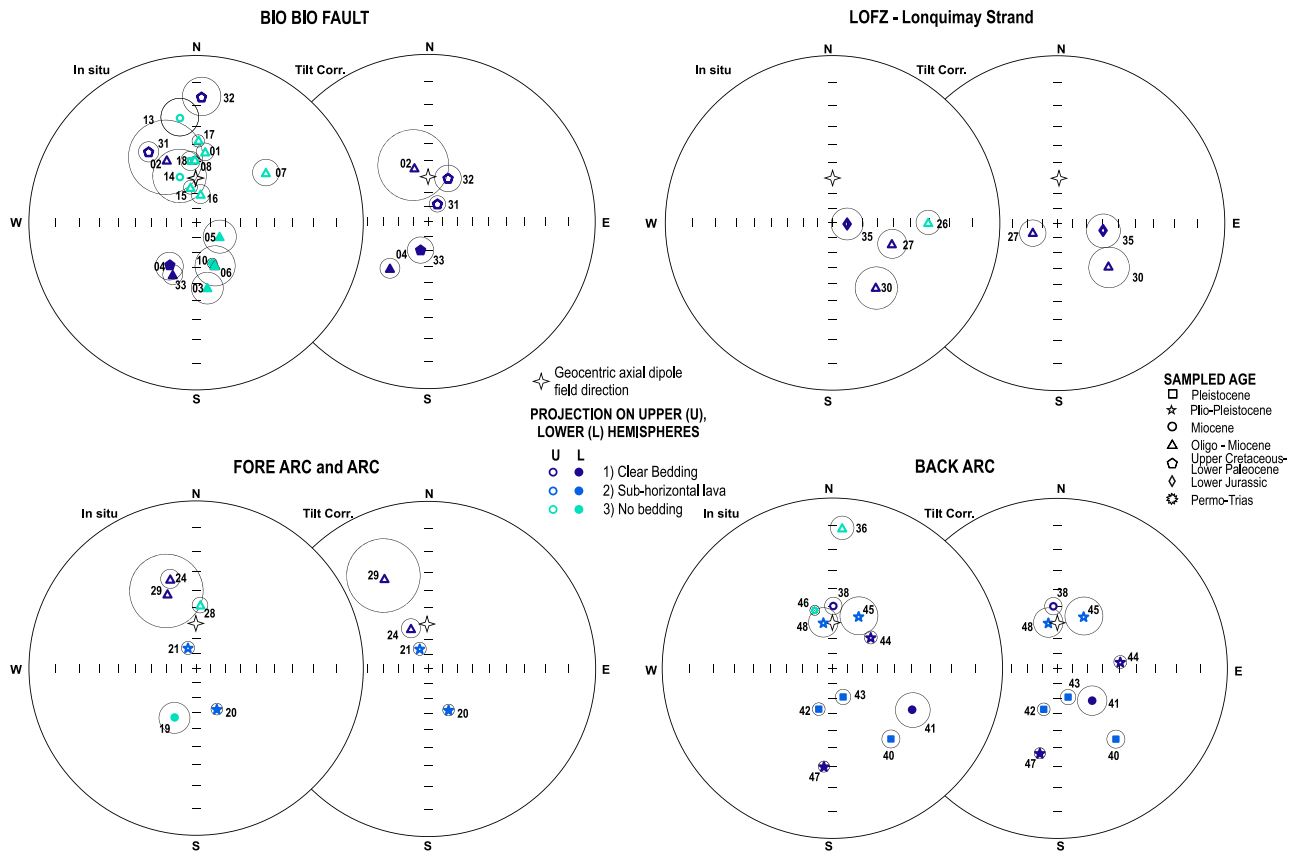
Figure 5. Equal angle projection of the site mean paleomagnetic directions gathered in the different domains of the study area. Symbols correspond to sites ages and are color coded by their reliability class related to bedding visibility in the sampling site. Solid and open symbols represent projection on the lower and upper hemisphere, respectively. Wider black circles are the projection of the α95 confidence cones.

Volcanic rocks emplaced during the transition of polarity reversals may be characterized by anomalously high PSV directional values (40–50° or more; e.g., Merrill et al., 1996). Sites recording such high PSV values likely fall among the four sites that do not match with the reliability criteria and that were rejected. The rotation values of the remaining 39 reliable sites may indeed have been biased as well by unrecognized PSV effects. However, there are two bits of evidence supporting a first-order validity of our data set for tectonic inferences: (1) PSV during a stable polarity state should mostly be in the 0–20° range that is a small value with respect to the tectonic rotations that along the LOFZ reach and probably exceed, 180° (e.g., Hernandez-Moreno et al., 2014; 2016); (2) data from the same structural domain yield a rather consistent pattern of CW (or CCW) rotations (Figure 2).

In addition, although it is well known that PSV represents a potential source of error when evaluating tectonic rotations of volcanic rocks, several paleomagnetic studies indeed used igneous rocks to unravel block rotation pattern, showing that PSV scatter may be validly averaged out by a significant number of sites (e.g., Piper et al., 1997; Marton et al., 2006; Gattacceca et al., 2007; Andreani et al., 2014; Hernandez-Moreno et al., 2014; 2016; Pellegrino et al., 2018, among many others).

8. Rotation Pattern

Rotation values with respect to South America are shown in Figure 2 and grouped according to the respective tectonic domain in Figure 6. Overall, clear bedding was apparent in 14 sites; seven sites were sampled in subhorizontal lava layers, and no bedding was apparent in the remaining eighteen sites (Table 1). The interpretation of the rotation pattern is strongly dependent upon such reliability criteria, as lack of bedding is one
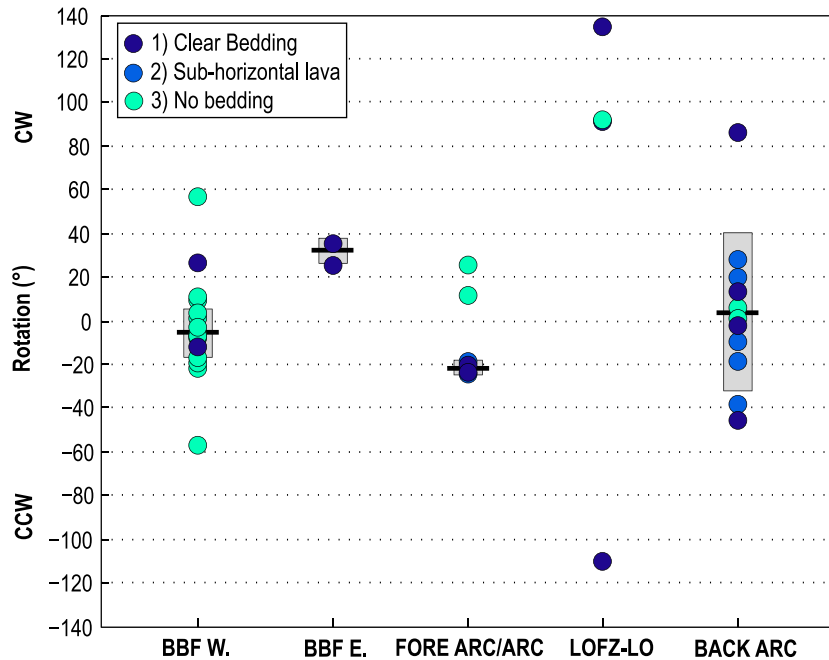
Figure 6. Paleomagnetic rotations with respect to South America grouped for each tectonic domain of the study area. Black thick lines indicate the mean rotation values for each domain; gray boxes are their standard deviation. Mean rotations from the fore-arc arc are calculated considering only sites of Class 1 with clear bedding.

of the main drawbacks of paleomagnetism applied to igneous rocks (Beck et al., 2000; Cembrano et al., 1992). Consequently, we mostly discarded sites of the lowest reliability Class 3.

Paleomagnetic rotations evaluated along the BBF show two different patterns; sites sampled in the western BBF portion (Figures 2a and 6) show limited rotation spread and overall insignificant rotations in both the normal ($R = -16.8° \pm 16.5°$) and reverse ($R = 18.3° \pm 20.8°$) polarity state ($R = -2.8° \pm 25°$ considering the whole data set), although we must acknowledge that bedding was not apparent at almost all sites. Conversely, sites sampled along the eastern BBF portion (BBF31–33) yield systematic CW rotations ranging from 25.4° to 35.8° (average 32.2° $\pm$ 5.8°).

Considering only the most reliable Class 1 and 2 sites, we obtain two different rotational behaviors in the fore-arc and arc regions. Sites from along the Tolhuaca strand of the LOFZ (i.e., sites BBF20, 21, 24, and 29) show a mean CCW rotation of 22.3° $\pm$ 2.7° (Figures 2b and 6). On the other hand, samples collected along the Lonquimay strand yield large CW rotations ranging from 90° to 134°, with the exception of site BBF27 showing a 110° CCW rotation (Figure 2b).

Finally, sites from the back-arc region are scattered with no apparent systematic rotation pattern (average rotation 3.9° $\pm$ 39.7°; Figures 2b and 6).

9. A Structural Model for the Northern LOFZ Termination

The paleomagnetic rotation pattern documented in this study shows that the main strike-slip faults crosscutting and bounding the Chiloé fore-arc sliver have very different tectonic characteristics and history. The BBF is considered to represent the northernmost of the sinistral NW trending strike-slip faults crossing the fore-arc (Mordojovich, 1981; Rapela and Pankrust, 1992; Bohm et al., 2002; Hackney et al., 2006; Rosenau et al., 2006). However, we could never recognize the BBF in the field, although a ~400 km long fault (e.g., Hackney et al., 2006) is expected to produce significant deformation in the host rocks and in the adjacent crust blocks. In this framework our new paleomagnetic data further help to understand BBF relevance and activity, as paleomagnetism is probably the best method for deciphering the kinematics of strike-slip fault-bounded blocks (e.g., McKenzie & Jackson, 1986; Ron et al., 1984; Sonder et al., 1994). Paleomagnetic data from the western BBF segment indicate unquestionably a lack of rotation, (mean rotation value is −5.6° ±

10.8°, excluding scattered directions from sites BBF04, 05, and 07; Figure 2a and 6). Although bedding was not apparent for the majority of the sites, the consistency of rotations from twelve sites is unquestionably a proof for dataset reliability (Figure 2a). We thus conclude that the BBF is an old tectonic feature, possibly Early Permian in age as suggested by Glodny et al. (2008) and that it did not play any relevant role during fore-arc sliver drift and deformation. Conversely, along the eastern BBF portion, east of the LOFZ (Figure 2b), we observed a low-angle SE dipping thrust fault together with highly inclined layers suggesting the occurrence of a NW verging thrust sheet (Figure 3a), and three sites from this area yielded a mean 32.2° ± 5.8° CW rotation (Figure 6). Such rotation pattern is not consistent with a supposed sinistral displacement along the BBF, because CCW rotations are expected to occur—considering the great majority of block rotation models—along left-lateral strike-slip faults (e.g., Hernández-Moreno et al., 2014).

Paleomagnetic data from the forearc and arc around the Tolhuaca strand of the LOFZ yield a well-defined CCW rotation of 22.3° ± 2.7° if only sites of Classes 1 and 2 are considered (Figure 6). Such homogeneous CCW pattern is not compatible with dextral displacement along the LOFZ that yields at 38–40°S latitudes large-magnitude CW rotations (e.g., Hernández-Moreno et al., 2014), but it is consistent with the CCW rotation pattern that was documented further south along the Chiloé fore-arc sliver (Hernández-Moreno et al., 2014, 2016). Therefore, we suggest that north of the Llaima volcano, the fault segment which we call Tolhuaca strand did not produce relevant displacement from at least the Oligo-Miocene (age of site BBF24) and it is not a LOFZ segment (Figure 7). Previous paleomagnetic data from the fore-arc region had showed a nearly ubiquitous CCW rotation pattern, with values ranging from 10° to 170° (Garcia et al., 1988; Cembrano et al., 1992; Rojas et al., 1994; Beck et al., 1988; 2000; Hernández-Moreno et al., 2014, 2016) that was related by Hernández-Moreno et al. (2014, 2016) to quasi-continuous crust deformation produced by the NW-SE left-lateral fault activity. Our new data seem to confirm this pattern and suggest that the fore-arc crust is dissected by closely spaced NW-SE trending faults, mostly hidden below glacial deposits and tephra and that the Tolhuaca strand does not belong to the LOFZ system, and its nature awaits further field investigations.

Along the Lonquimay strand, we observed fault zones where intense deformation is localized in a few tens of meters (Figures 3g–3i). Near-vertical and straight fault planes are the typical expression of the LOFZ and strike-slip kinematic indicators point to dextral horizontal displacement (Figure 3l). Here, two sites with clear bedding yield 90° and 135° CW rotation, while 14 km to the south site BBF27 shows a 110° CCW rotation. We explain such rotational inconsistency hypothesizing that the apparent 110° CCW rotation is, in fact, a 290° CW rotation, as also supposed by Hernández-Moreno et al. (2014) for few sites apparently yielding a CCW rotation further south along the LOFZ, dominated by high-magnitude (up to 170°) CW-rotated sites. Consistent CW rotation is also observed along the supposed eastern segment of the BBF. Three sites sampled north of the Lonquimay strand close to Troyo display a mean 32.2° ± 5.8° CW rotation (Figure 6), which, as discussed above is inconsistent with sinistral displacement along the BBF. Combining these data together, the CW rotation pattern is clear and suggests that (1) the LOFZ runs along the Lonquimay strand and that (2) the three sites north of the Lonquimay strand are under the tectonic influence of the LOFZ northern end instead of that the BBF. The amount of CW rotation appears to decrease moving northward from site BBF30 to BBF31 (Figure 7). Consistently, field observations highlight a progressive increase of slickenlines pitch (Figures 3l–3n, site BBF35), and increasing bedding dip moving northward, together with low-angle reverse faults (Figures 3a and 3b). Overall, such data suggest that transpressive deformation becomes dominant over pure strike-slip displacement at the northern LOFZ end (Figure 7). Such pattern is consistent with recent seismic evidence (Sielfeld et al., 2019), showing splay faulting along the LOFZ at these latitudes and further north. North of the Copahue volcano, the NE trending Copahue-Antiñir fault crosses the main Cordillera toward the NE and becomes the external accretionary front of the Andes between 37°S and 38°S. This system has been inferred to be a transfer zone from the dominant strike-slip deformation in the south to a purely compressive Andean front in the north, in agreement with our data (Folguera et al., 2004; Figure 7).

The rotation pattern in the backarc is less clear. Retaining only the Classes 1 and 2 paleomagnetic directions, the mean rotation value is 3.9° ± 39.7°. As sites from the backarc were all sampled in volcanic rocks, the observed scatter of paleomagnetic rotations could be due to the PSV of the geomagnetic field and/or unrecognized local tectonics.
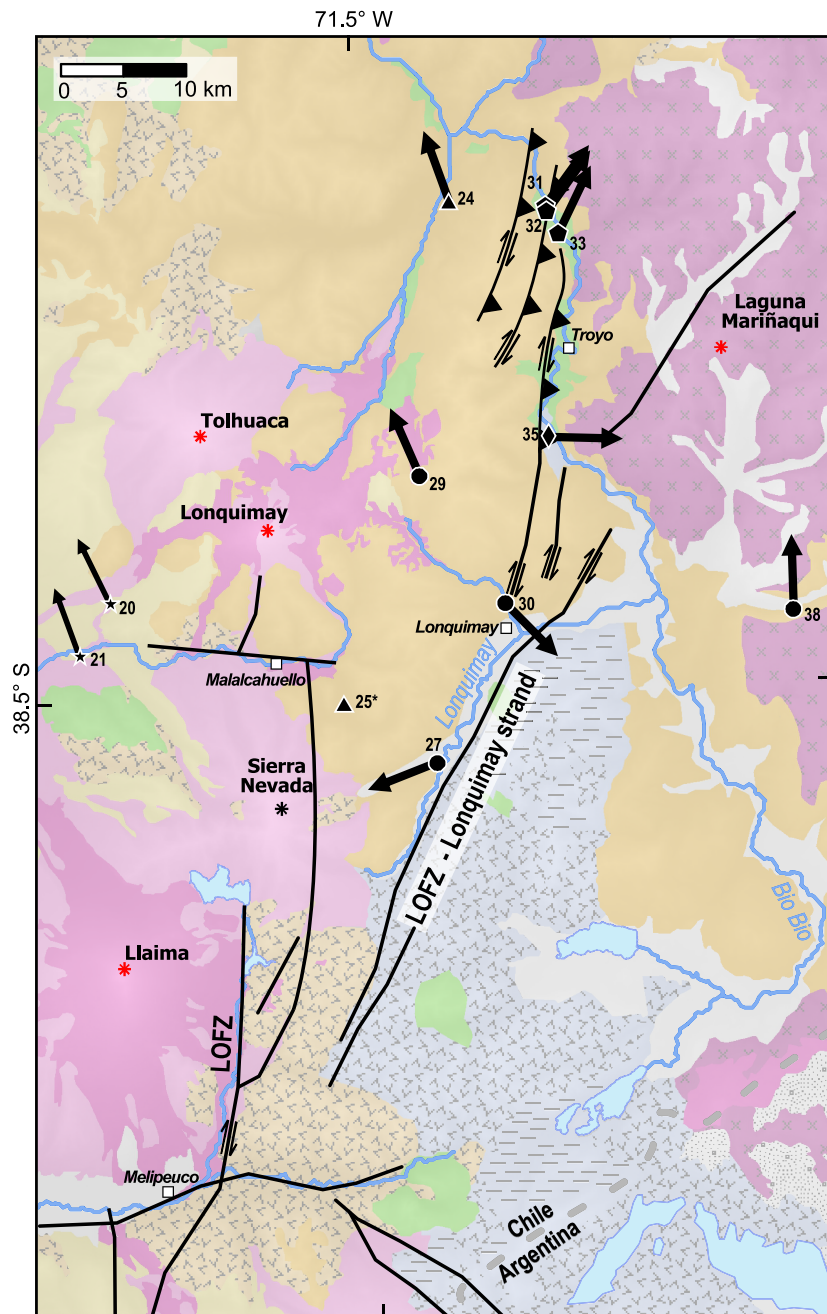
Figure 7. Structural model of the northern LOFZ termination inferred from our field and class 1 paleomagnetic data. For legend refer to Figure 2.

Most of our sites are Oligo-Miocene in age, implying that our data are not useful to constrain the age of forearc and arc deformation better than those by Hernández-Moreno et al. (2014, 2016), who showed that rotations are post-5 Ma and that the occurrence of older rotation cannot be properly evaluated.

In summary, our data reveal an unexpected fault geometry and kinematics along the northern LOFZ end. We suggest that the LOFZ runs solely along the Lonquimay valley, while the so-called Tolhuaca strand is, in fact, a crust discontinuity of unclear nature and is not characterized by significant dextral displacement (Figure 7). In the northern LOFZ termination, the strike-slip component decreases turning into a transpressional domain and to the Copahue-Antiñir fault that further north turns into the compressive accretionary front of the Andes (Folguera et al., 2004). Field and paleomagnetic data gathered along the western BBF

segment instead show that such fault has not yielded significant tectonic deformation and rotation so that its real occurrence is questionable. The scattered rotations observed in the back-arc region conversely do not indicate any clear influence of tectonics (if existing) to the paleomagnetic pattern.

10. Orogen-Parallel Transition From a Decoupled Fore-Arc Sliver to Andean-Type Mountain Chain

Our and previous paleomagnetic data from the Chiloé sliver (Garcia et al., 1988; Cembrano et al., 1992; Rojas et al., 1994; Beck, 1988, 1991; Beck et al., 2000; Hernández-Moreno et al., 2014; 2016) show that the forearc is characterized by ubiquitous CCW rotations with respect to South America, likely related to deformation and rotation along sinistral SW-NE faults. On the other hand, the LOFZ deformation zone displays >90° CW rotations and diffuse upper crust fragmentation. However, the interaction between the LOFZ and the sinistral transverse faults crossing the sliver is still speculative. Previous studies related the transverse NW-SE structures and the LOFZ (Beck et al., 1993; Rosenau et al., 2006), although more recent data seem to be at odds with such model (e.g., Hernández-Moreno et al., 2014).

At the regional scale, the dextral LOFZ displacement implies northward Chiloé block drift that is clearly imaged by GPS data (Klotz et al., 2001; Wang et al., 2007; Ruegg et al., 2009; Moreno et al., 2011; Figure 1 b). Consistently, extension occurs at the southern LOFZ end, yielding the formation of the Golfo de Peñas-Taito pull-apart basin (Forsythe & Nelson, 1985). Toward the north, instead, the concurrence of dextral displacement along the LOFZ and sinistral displacement along the transverse faults that terminate against the LOFZ (according to the paleomagnetic data by Hernández-Moreno et al., 2014) requires that (1) extension occurs just north of the branching of each sinistral fault with the LOFZ; (2) such extended crust is "filled" by dextral LOFZ displacement that generates crust squeezing and progressive accretion of small crust blocks within the fault damage zone (Figure 8). Despite the lack of significant field evidence from the fore-arc region, the paleomagnetic data by Hernández-Moreno et al. (2014, 2016) clearly show that the upper crust near the LOFZ trace is fragmented in 1–10 km wide rotating crustal blocks and highlights the further occurrence of elongated blocks, whose rotation is prevented by their aspect ratio. Such blocks are translated parallel to the fault trace from at least the Oligo-Miocene, considering the age of the sampled rocks. This would imply a constant accretion of material and a continuous northward push that could have driven preexisting NW-SE crustal discontinuities to reactivate (Figure 8), accommodating part of the margin parallel strain coming from the Nazca plate oblique subduction. Consistently, margin-parallel shortening in the fore-arc region led to the formation of the Nahuelbuta Range from the early Pliocene (Melnick et al., 2009).

Our tectonic model is not at odds with previous inferences by Hernández-Moreno et al. (2016), who suggested that the relative activity of the transverse faults and the LOFZ is a function of plate coupling along the subduction interface. Patches of high plate coupling would enhance stress normal to the LOFZ and thus higher deformation and CW rotations just west of the LOFZ in the fore-arc sliver. On the contrary, low plate coupling would imply a weaker LOFZ and smaller damage zone and CW rotations, thus favoring sinistral shear along the transverse faults and prevailing CCW rotations in the forearc. Thus, variation in time and space of plate coupling could control the long-term evolution of the fore-arc integrated fault system.

Our paleomagnetic data also suggest that strain partitioning of the oblique subduction is limited to the Andean margin south of ~38°S. The LOFZ ends with transpressional structures yielding moderate (~30°) CW rotations, while further north the Antiñir-Copahue transverse zone shifts the deformation to the active Andean accretion front (Figure 8). Consistently, temporary seismic arrays indicate splay faulting at the northern LOFZ termination (Sielfeld et al., 2019).

We also show that the BBF did not produce significant deformation (and block rotation) from the Late Oligocene onward. Thus, the BBF appears to represent just the northern boundary of the Chiloé fore-arc sliver, north of which no further NW-SE transverse sinistral faults are observed (e.g., Hackney et al., 2006). At the same latitude along the coastal domain the Nahuelbuta Range (Figure 1) has been uplifted as consequence of localized margin-parallel shortening in response to northward translation of the Chiloé fore-arc sliver against a crust buttress (Melnick et al., 2009). The Nahuelbuta Range possibly marks the northern end of the Chiloé sliver in the fore arc domain and is therefore consistent with our model.
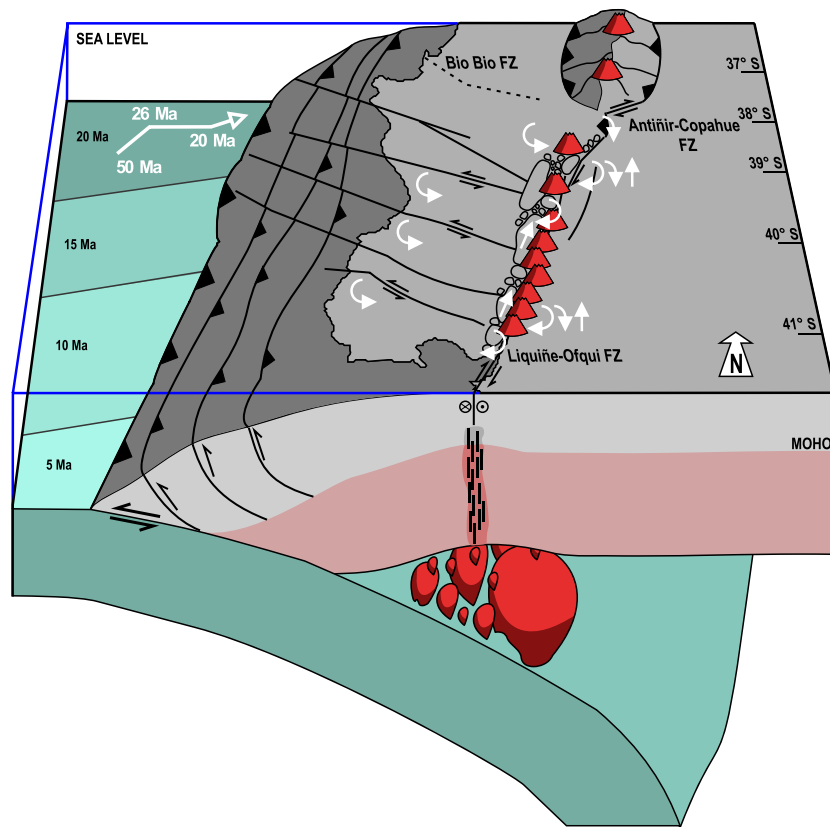
Figure 8. Crustal-scale sketch of the subduction system in southern Chile between 37°S and 41°S. White curved arrows indicate average sense and amount of paleomagnetic rotations; straight white arrows indicate no rotation; red cones represent Quaternary volcanoes. The continuous push of northward translated crust material along the LOFZ damage zone reactivates the transverse faults of the forearc with sinistral displacement. We speculate that fore-arc sliver ends at 38°S because older age of subducting Nazca plates transfers less heat to the upper plate increasing its rigidity and inhibiting crust detachment.

Flat-slab subduction and thick central Andean crust have been advocated as strain-partitioning preventing factors (Rosenau et al., 2006; Siame et al., 2005). However, both of them occurs far away from the northern termination of the LOFZ, flat slab occurring north of ~35°S (e.g., Espurt et al., 2008) and the thick central Andean crust being documented north of 33°S (Gimenez et al., 2019). Therefore, other factors determining the northward end of strain partitioning must exist, such as crust temperature gradient and a northward along-strike decrease of the total heat budget in the crust. Indeed, the LOFZ constantly follows the volcanic arc, likely because this is the weakest part of the upper plate crust (Cembrano & Lara, 2009; Lara et al., 2004). However, the volcanic arc extends outward from the LOFZ trace, both to the south and to the north (e.g., Cembrano & Lara, 2009); thus, it possibly plays a small role in the upper crust strain distribution. Other sources of heat could come from the lower plate. For instance, the subduction of several segments of the Chile rise below South America at ~48°S (Cande & Leslie, 1986; Murdie et al., 1993; Nelson et al., 1993) was inferred to represent a significant driving force sustaining the late Cenozoic dextral transpressional deformation and crust exhumation along the southern LOFZ segment (Forsythe & Nelson, 1985; Thomson, 2002). Here, an anomalous Late-Cenozoic heat flow was deduced from very young thermochronologic ages (Thomson, 2002). Presently, at ~48°S the triple junction between Nazca, Antarctica, and South America marks the ongoing subduction of the Chile rise. Moving northward, the age of the subducting Nazca plate increases (Müller et al., 2008; Figure 8), implying a progressive crust temperature decrease at the trench. Thus, we suggest that the occurrence of strain partitioning along the Nazca subduction system between 48°S and 38°S could be related to the temperature structure of the lower-upper plate combined system and that a heat budget gradient could be responsible for the northward transition from a strike-slip dominated deformation front (i.e., the LOFZ) to the purely accretionary Andean front (Figure 8).

11. Conclusions

Our work proves that paleomagnetism may provide fundamental evidence to unravel crust setting where the bedrock geology is masked by alluvial, glacial, or volcanic/volcanoclastic cover. We show that the BBF, supposedly the northernmost of the sinistral NW-SE faults crosscutting the Chiloé fore-arc sliver, did produce in fact neither significant deformation nor paleomagnetic rotations from Late Oligocene onward. We conclude that the BBF is just the undeformed northern boundary of the Chiloé sliver. Further south, CCW rotations in the fore-arc domain confirm previous results and are consistently related to sinistral displacement along frequently hidden NW-SE faults. CCW rotations also observed along a supposed western LOFZ segment (Tolhuaca strand) do not support its dextral displacement and suggest that such crust discontinuity does not represent a LOFZ strand. Further east, 90–130° CW rotations and strong tectonic deformation are observed along the eastern LOFZ segment (Lonquimay strand) clearly showing LOFZ occurrence and dextral shear. Rotation amount decreases moving northward along the Lonquimay strand and at 38.1°S latitudes is reduced to 32° ± 5.8° CW, where the LOFZ becomes a dextral transpressive fault. The LOFZ northern termination occurs where it crosses the inactive BBF trace. Further north, the Antiñir-Copahue fault system is the transitional link from strain partitioning due to the oblique convergence to purely compressive deformation occurring at the Andes front north of 38°S.

We speculate that the activity of the LOFZ and of the transverse faults crosscutting the Chiloé sliver is connected, as crust pushed northward by LOFZ shear and squeezed via block fragmentation/rotation escapes toward the trench reactivating preexisting NW-SE faults with sinistral displacement. We also suggest that the main factor controlling the northward transition from a fully detached fore-arc sliver to Andean-type mountain chain is the total heat budget in the coupled lower-upper plate system. At the southern LOFZ end, the subduction of the Chile rise gives large heat input to the upper plate, sustaining Cenozoic dextral shear and exhumation. The northward increasing age of the subducting Nazca plate implies progressive decrease of upper plate heating, in turn determining a reduction of crust weakness and attitude to host regional crustal discontinuities (i.e., the LOFZ), eventually favoring a transition from strike-slip to compressional deformation.

References

Adriasola, A. C., Thomson, S. N., Brix, M. R., Hervé, F., & Stöckhert, B. (2006). Postmagmatic cooling and late Cenozoic denudation of the North Patagonian Batholith in the Los Lagos region of Chile, 41– 42 15′ S. *International Journal of Earth Sciences*, *95*(3), 504–528.

Andreani, L., Gattacceca, J., Rangin, C., Martinez-Reynez, J., & Demory, F. (2014). Counterclockwise rotations in the Late Eocene–Oligocene volcanic fields of San Luis Potosí and Sierra de Guanajuato (eastern Mesa Central, Mexico). *Tectonophysics*, *637*, 289–304.

Angermann, D., Klotz, J., & Reigber, C. (1999). Space-geodetic estimation of the Nazca-South America Euler vector. *Earth and Planetary Science Letters*, *171*(3), 329–334.

Barrientos, S., & Acevedo-Aránguiz, P. (1992). Seismological aspects of the 1988–1989 Lonquimay (Chile) volcanic eruption. *Journal of Volcanology and Geothermal Research*, *53*, 73–87.

Beck, M. Jr., Burmester, R., Cembrano, J., Drake, R., García, A., Hervé, F., & Munizaga, F. (2000). Paleomagnetism of the North Patagonian Batholith, southern Chile. An exercise in shape analysis. *Tectonophysics*, *326*(1-2), 185–202.

Beck, M., Rojas, C., & Cembrano, J. (1993). On the nature of buttressing in margin-parallel strike-slip fault systems. *Geology*, *21*, 755–758. https://doi.org/10.1130/0091-7613(1993)021<0755

Beck, M. E. (1980). Paleomagnetic record of plate-margin tectonic processes along the western edge of North America. *Journal of Geophysical Research*, *85*(80), 7115–7131. https://doi.org/10.1029/JB085iB12p07115

Beck, M. E. Jr. (1988). Analysis of Late Jurassic-Recent paleomagnetic data from active plate margins of South America. *Journal of South American Earth Sciences*, *1*(1), 39–52.

Beck, M. E. Jr. (1991). Coastwise transport reconsidered: Lateral displacements in oblique subduction zones, and tectonic consequences. *Physics of the Earth and Planetary Interiors*, *68*(1-2), 1–8.

Bohm, M., Lüth, S., Echtler, H., Asch, G., & Bataille, K. (2002). The Southern Andes between 36° and 40°S latitude: Seismicity and average seismic velocities. *Tectonophysics*, *356*, 275–289.

Cande, S., & Leslie, R. (1986). Late Cenozoic tectonics of the southern Chile trench. *Journal of Geophysical Research*, *91*(B1), 471–496. https://doi.org/10.1029/JB091iB01p00471

Cembrano, J., Beck, M. E. Jr., Burmester, R. F., Rojas, C., Garcia, A., & Herve, F. (1992). Paleomagnetism of lower Cretaceous rocks from east of the Liquiñe-Ofqui fault zone, southern Chile: Evidence of small in-situ clockwise rotations. *Earth and Planetary Science Letters*, *113*(4), 539–551.

Cembrano, J., & Hervé, F. (1993). The Liquine Ofqui Fault Zone: A major Cenozoic strike slip duplex in the Southern Andes, Second ISAG, International Symposium Andean geodynamics: extended abstracts. Paris, ORSTOM, pp. 175–178. ISBN 2-7099-1154-X

Cembrano, J., Hervé, F., & Lavenu, A. (1996). The Liquiñe Ofqui fault zone: A long-lived intra-arc fault system in southern Chile. *Tectonophysics*, *259*(1-3), 55–66.

Cembrano, J., & Lara, L. (2009). The link between volcanism and tectonics in the southern volcanic zone of the Chilean Andes: A review. *Tectonophysics*, *471*(1–2), 96–113. https://doi.org/10.1016/j.tecto.2009.02.038

Cembrano, J., Lavenu, A., Reynolds, P., Arancibia, G., López, G., & Sanhueza, A. (2002). Late Cenozoic transpressional ductile deformation north of the Nazca–South America–Antarctica triple junction. *Tectonophysics*, *354*(3-4), 289–314.

Cembrano, J., Schermer, E., Lavenu, A., Hervé, F., Barrientos, S., McClelland, B., & Arancibia, G. (1996). *Nature and timing of Cenozoic intra-arc deformation, southern Chile, paper presented at Third ISAG, St.* France: Malo.

Cembrano, J., Schermer, E., Lavenu, A., & Sanhueza, A. (2000). Contrasting nature of deformation along an intra-arc shear zone, the Liquiñe–Ofqui fault zone, southern Chilean Andes. *Tectonophysics, 319*(2), 129–149.

Chinn, D., & Isacks, B. (1983). Accurate source depths and focal mechanisms of shallow earthquakes in western South America and in the New Hebrides island arc. *Tectonics, 2*(6), 529–563. https://doi.org/10.1029/TC002i006p00529

Cifuentes, I. N. I. S. L. (1989). The 1960 Chilean Earthquakes. *Journal of Geophysical Ressearch., 94*(B1), 665–680. https://doi.org/10.1029/JB094iB01p00665

Demarest, H. (1983). Error analysis for the determination of tectonic rotation from paleomagnetic data. *Journal of Geophysical Research, 88*(B5), 4321–4328. https://doi.org/10.1029/JB088iB05p04321

Dewey, J. F., & Lamb, S. H. (1992). Active tectonics of the Andes, Tectonophysics, 205(1–3), 79–95, doi:10.1016/0040-1951(92)90419-7. Murdie, R., D. Prior, P. Styles, S. Flint, R. Pearce, and S. Agar (1993), Seismic responses to ridge-transform subduction: Chile triple junction. *Geology, 21*(12), 1095–1098. https://doi.org/10.1130/0091-7613(1993)021<1095

Dziewonski, A. M., Ekström, G., Woodhouse, J. H., & Zwart, G. (1991). Centroid-moment tensor solutions for April June 1990. *Physics of the Earth and Planetary Interiors, 66*(3), 133–143.

Espurt, N., Funiciello, F., Martinod, J., Guillaume, B., Regard, V., Faccenna, C., & Brusset, S. (2008). Flat subduction dynamics and deformation of the South American plate: Insights from analog modeling. *Tectonics, 27*, TC3011. https://doi.org/10.1029/2007tc002175

Fisher, R. A. (1953). Dispersion on a sphere, Proc. R. Soc. London, Ser. A, *217*, 295–305.

Fitch, T. (1972). Plate convergence, transcurrent faults, and internal deformation adjacent to southeast Asia and the western Pacific. *Journal of Geophysical Research, 77*(23), 4432–4460. https://doi.org/10.1029/JB077i023p04432

Folguera, A., Ramos, V. A., Hermanns, R. L., & Naranjo, J. (2004). Neotectonics in the foothills of the southernmost central Andes (37°–38° S): Evidence of strike-slip displacement along the Antiñir-Copahue fault zone. *Tectonics, 23*, TC5008, https://doi.org/10.1029/2003tc001533

Forsythe, R., & Nelson, E. (1985). Geological manifestations of ridge collision: Evidence from the Golfo de Penas-Taitao Basin, southern Chile. *Tectonics, 4*(5), 477–495.

Garcia, A., Beck, M., Burmester, R., Munizaga, F., & Herve, F. (1988). Paleomagnetic reconnaissance of the Region de Los Lagos, southern Chile, and its tectonic implications. *Revista Geológica de Chile v, 15*(1), 13–30. https://doi.org/10.5027/andgeoV15n1-a02

Gattacceca, J., Deino, A., Rizzo, R., Jones, D. S., Henry, B., Beaudoin, B., & Vadeboin, F. (2007). Miocene rotation of Sardinia: New paleomagnetic and geochronological constraints and geodynamic implications, Earth Planet. *Science Letters, 258*, 359–377. https://doi.org/10.1016/j.epsl.2007.02.003

Gimenez, M., Pesce, A., Pechuan, S., Arecco, M. A., Soler, S. R., Otto, S. C., et al. (2019). Crustal structure in the southern Andes, adjacent foreland, and Atlantic passive margin delineated by satellite gravimetric models. In Andean Tectonics (pp. 557-572). Elsevier.

Glodny, J., Echtler, H., Collao, S., Ardiles, M., Burón, P., & Figueroa, O. (2008). Differential late Paleozoic active margin evolution in South-Central Chile (37°S–40°S)—The Lanalhue Fault Zone. *Journal of South American Earth Sciences, 26*(4), 397–411.

Haberland, C., Rietbrock, A., Lange, D., Bataille, K., & Hofmann, S. (2006). Interaction between forearc and oceanic plate at the south-central Chilean margin as seen in local seismic data. *Geophysical Research Letters, 33*, L23302. https://doi.org/10.1029/2006GL028189

Hackney, R. I., Echtler, H. P., Franz, G., Götze, H. J., Lucassen, F., Marchenko, D., Melnick, D, Meyer, U, Schmidt, S, & Tassara, A. (2006). The segmented overriding plate and coupling at the south-central Chilean margin (36–42°S). *In The Andes (pp. 355-374).* Springer, Berlin, Heidelberg.

Hernández-Moreno, C., Speranza, F., & Di Chiara, A. (2014). Understanding kinematics of intra-arc transcurrent deformation: Paleomagnetic evidence from the Liquiñe-Ofqui fault zone (Chile, 38–41° S). *Tectonics, 33*, 1964–1988.

Hernández-Moreno, C., Speranza, F., & Di Chiara, A. (2016). Paleomagnetic rotation pattern of the southern Chile fore-arc sliver (38°S–42° S): A new tool to evaluate plate locking along subduction zones. *Journal of Geophysical Research: Solid Earth, 121*, 469–490.

Hervé, F. (1994). *The southern Andes between 39 and 44 S latitude: The geological signature of a transpressive tectonic regime related to a magmatic arc, In Tectonics of the Southern Central Andes (pp. 243-248), ().* Berlin, Heidelberg: Springer.

Hervé, M. (1976). Estudio geologico de la falla Liquine-Reloncavi en el area de Liquine: antecedentes de un movimiento transcurrente (Provincia de Valdivia). *Actas Congr. Geol. Chil, 1*, B39–B56.

Howell, J. A., Schwarz, E., Spalletti, L. A., & Veiga, G. D. (2005). The Neuquén basin: An overview. *Geological Society, London, Special Publications, 252*(1), 1–14.

Hu, Y., Wang, K., He, J., Klotz, J., & Khazaradze, G. (2004). Three-dimensional viscoelastic finite element model for postseismic deformation of the great 1960 Chile earthquake. *Journal of Geophysical Research - Solid Earth, 109*(B12).

Katili, J. A. (1970). Large transcurrent faults in southeast Asia with special reference to Indonesia. *Geologische Rundschau, 59*, 581–600.

Kendrick, E., Bevis, M., Smalley, R. Jr., Brooks, B., Vargas, R. B., Lauría, E., & Fortes, L. P. S. (2003). The Nazca–South America Euler vector and its rate of change. *Journal of South American Earth Sciences, 16*(2), 125–131.

Khazaradze, G., Wang, K., Klotz, J., Hu, Y., & He, J. (2002). Prolonged post-seismic deformation of the 1960 great Chile earthquake and implications for mantle rheology. *Geophysical Research Letters, 29*(22), 2050. https://doi.org/10.1029/2002gl015986

Kimura, H., Ishikawa, N., & Sato, H. (2011). Estimation of total lateral displacement including strike–slip offset and broader drag deformation on an active fault: Tectonic geomorphic and paleomagnetic evidence on the Tanna fault zone in central Japan. *Tectonophysics, 501*(1–4), 87–97. https://doi.org/10.1016/j.tecto.2011.01.016

Kimura, H., Itoh, Y., & Tsutsumi, H. (2004). Quaternary strike-slip crustal deformation around an active fault based on paleomagnetic analysis: A case study of the Enako fault in central Japan. *Earth and Planetary Science Letters, 226*(3–4), 321–334, https://doi.org/10.1016/j.epsl.2004.08.003

Kirschvink, J. L. (1980). The least-squares line and plane and the analysis of paleomagnetic data. *Geophysical Journal of the Royal Astronomical Society, 62*(3), 699–718.

Klotz, J., Khazaradze, G., Angermann, D., Reigber, C., Perdomo, R., & Cifuentes, O. (2001). Earthquake cycle dominates contemporary crustal deformation in Central and Southern Andes. *Earth and Planetary Science Letters, 193*(3-4), 437–446.

Lamb, S. H. (1987). A model for tectonic rotations about a vertical axis. *Earth and Planetary Science Letters, 84*(1), 75–86. https://doi.org/10.1016/0012-821X(87)90178-6

Lange, D., Cembrano, J., Rietbrock, A., Haberland, C., Dahm, T., & Bataille, K. (2008). First seismic record for intra-arc strike-slip tectonics along the Liquiñe-Ofqui fault zone at the obliquely convergent plate margin of the southern Andes. *Tectonophysics, 455*(1–4), 14–24. https://doi.org/10.1016/j.tecto.2008.04.014

Lara, L. E., Cembrano, J., Lavenu, A., & Darrozes, J. (2004). Monogenetic volcanoes in Southern Andes and their relationship with vertical displacements along major strike-slip intra-arc faults, in. *IAVCEI General Assembly*, *104*.

Lavenu, A., & Cembrano, J. (1999). Compressional-and transpressional-stress pattern for Pliocene and Quaternary brittle deformation in fore arc and intra-arc zones (Andes of Central and Southern Chile). *Journal of Structural Geology*, *21*(12), 1669–1691.

Lear, C. H., Elderfield, H., & Wilson, P. A. (2000). Cenozoic deep-sea temperatures and global ice volumes from Mg/Ca in benthic foraminiferal calcite. *Science*, *287*(5451), 269–272. https://doi.org/10.1126/science.287.5451.269

Lonsdale, P. (2005). Creation of the Cocos and Nazca plates by fission of the Farallon plate. *Tectonophysics*, *404*(3), 237–264.

López-Escobar, L., Cembrano, J., & Moreno, H. (1995). Geochemistry and tectonics of the Chilean Southern Andes, Andean. *Geology*, *22*(2). https://doi.org/10.5027/andgeoV22n2-a06

Marton, E., Trajanova, M., Zupancic, N., & Jelen, B. (2006). Formation, uplift and tectonic integration of a Periadriatic intrusive complex (Pohorje, Slovenia) as reflected in magnetic parameters and palaeomagnetic directions. *Geophysical Journal International*, *167*, 1148–1159.

McCaffrey, R. (2008). Global frequency of magnitude 9 earthquakes. *Geology*, *36*(3), 263–266.

McFadden, P. L. (1990). A new fold test for palaeomagnetic studies. *Geophysical Journal International*, *103*(1), 163–169.

McFadden, P. L., & McElhinny, M. W. (1990). Classification of the reversal test in palaeomagnetism. *Geophysical Journal International*, *103*(3), 725–729.

McKenzie, D., & Jackson, J. (1983). The relationship between strain rates, crustal thickening, palaeomagnetism, finite strain and fault movements within a deforming zone. *Earth and Planetary Science Letters*, *65*(1), 182–202.

McKenzie, D., & Jackson, J. (1986). A block model of distributed deformation by faulting. *Journal of the Geological Society of London*, *143*(2), 349–353. https://doi.org/10.1144/gsjgs.143.2.0349

Melnick, D., Bookhagen, B., Echtler, H. P., & Strecker, M. R. (2006). Coastal deformation and great subduction earthquakes, Isla Santa María, Chile (37 S). *Geological Society of America Bulletin*, *118*(11-12), 1463–1480.

Melnick, D., Bookhagen, B., Strecker, M. R., & Echtler, H. P. (2009). Segmentation of megathrust rupture zones from fore-arc deformation patterns over hundreds to millions of years, Arauco peninsula, Chile. *Journal of Geophysical Research - Solid Earth*, *114*(B1).

Melnick, D., & Echtler, H. P. (2006). Inversion of forearc basins in south-central Chile caused by rapid glacial aPleistocene glacial depositge trench fill. *Geology*, *34*(9), 709–712.

Merrill, R. T., McElhinny, M. W., & McFadden, P. L. (1996). *The magnetic field of the Earth: Paleomagnetism, the Core, and the Deep Mantle*. New York: Elsevier.

Mordojovich, C. (1981). Sedimentary basins of Chilean Pacific offshore. In M. T. Halbouty (Ed.), *Energy Resources of the Pacific Region* (pp. 63–82). American Association of Petroleum Geologists, Tulsa, OK, USA: AAPG Studies in Geology.

Moreno, M., Melnick, D., Rosenau, M., Bolte, J., Klotz, J., Echtler, H., et al. (2011). Heterogeneous plate locking in the South–Central Chile subduction zone: Building up the next great earthquake. *Earth and Planetary Science Letters*, *305*(3-4), 413–424.

Müller, R. D., Sdrolias, M., Gaina, C., & Roest, W. R. (2008). Age, spreading rates, and spreading asymmetry of the world's ocean crust. *Geochemistry, Geophysics, Geosystems*, *9*, Q04006. https://doi.org/10.1029/2007gc001743

Muñoz, J., & Stern, C. R. (1988). The Quaternary volcanic belt of the southern continental margin of South America: Transverse structural and petrochemical variations across the segment between 38°S and 39°S. *Journal of South American Earth Sciences*, *1*(2), 147–161.

Muñoz, J. B., & Stern, C. R. (1989). Alkaline magmatism within the segment 38°–39°S of the Plio-Quaternary Volcanic Belt of the southern South American Continental Margin. *Journal of Geophysical Research - Solid Earth*, *94*(B4), 4545–4560.

Murdie, R., Prior, D., Styles, P., Flint, S., Pearce, R., & Agar, S. (1993). Seismic responses to ridge-transform subduction: Chile triple junction. *Geology*, *21*(12), 1095–1098. https://doi.org/10.1130/0091-7613(1993)021<1095

Murdie, R. E. (1994), Seismicity and Neotectonics associated with the subduction of an active ocean ridge transform system Southern Chile, PhD thesis, Univ. of Liverpool.

Nelson, E., Forsythe, R., Diemer, J., Allen, M., & Urbina, O. (1993). Taitao ophiolite: A ridge collision ophiolite in the forearc of southern Chile (46°S). *Revista Geologica de Chile*, *20*, 137.

Nelson, M. R., & Jones, C. H. (1987). Paleomagnetism and crustal rotations along a shear zone, Las Vegas Range, southern Nevada. *Tectonics*, *6*(1), 13–33.

Nocquet, J. M., Villegas-Lanza, J. C., Chlieh, M., Mothes, P. A., Rolandone, F., Jarrin, P., et al. (2014). Motion of continental slivers and creeping subduction in the northern Andes. *Nature Geoscience*, *7*(4), 287.

Pardo-Casas, F., & Molnar, P. (1987). Relative motion of the Nazca (Farallon) and South American plates since Late Cretaceous time. *Tectonics*, *6*(3), 233–248.

Pellegrino, A. G., Zhang, B., Speranza, F., Maniscalco, R., Yin, C., Hernandez-Moreno, C., & Winkler, A. (2018). Tectonics and paleomagnetic rotation pattern of Yunnan (24°N–25°N, China): Gaoligong Fault Shear Versus Megablock Drift. *Tectonics*, *37*(5), 1524-1551.

Piper, J. D. A., Tatar, O., & Gürsoy, H. (1997). Deformational behaviour of continental lithosphere deduced from block rotations across the North Anatolian fault zone in Turkey. *Earth and Planetary Science Letters*, *150*(3-4), 191–203.

Plafker, G., & Savage, J. C. (1970). Mechanism of the Chilean earthquakes of May 21 and 22, 1960. *Geological Society of America Bulletin*, *81*(4), 1001–1030.

Quinteros, J., & Sobolev, S. V. (2013). Why has the Nazca plate slowed since the Neogene? *Geology*, *41*(1), 31–34.

Randall, K., Lamb, S., & Mac Niocaill, C. (2011). Large tectonic rotations in a wide zone of Neogene distributed dextral shear, northeastern South Island, New Zealand. *Tectonophysics*, *509*(3-4), 165–180.

Rapela, C. W., & Pankhurst, R. J. (1992). The granites of northern Patagonia and the Gastre Fault System in relation to the break-up of Gondwana. *Geological Society, London, Special Publications*, *68*(1), 209–220.

Rojas, C., Beck, M., & Burmester, R. (1994). Paleomagnetism of the mid-Tertiary Ayacara Formation, southern Chile: Counterclockwise rotation in a dextral shear zone. *Journal of South American Earth Sciences*, *7*(1), 45–56.

Ron, H., Freund, R., Garfunkel, Z., & Nur, A. (1984). Block rotation by strike-slip faulting: Structural and paleomagnetic evidence. *Journal of Geophysical Research*, *89*(B7), 6256–6270. https://doi.org/10.1029/JB089iB07p06256

Rosenau, M., Melnick, D., & Echtler, H. (2006). Kinematic constraints on intra-arc shear and strain partitioning in the southern Andes between 38°S and 42°S latitude. *Tectonics*, *25*, TC4013. https://doi.org/10.1029/2005TC001943

Ruegg, J. C., Rudloff, A., Vigny, C., Madariaga, R., De Chabalier, J. B., Campos, J., et al. (2009). Interseismic strain accumulation measured by GPS in the seismic gap between Constitución and Concepción in Chile. *Physics of the Earth and Planetary Interiors*, *175*(1-2), 78–85.

Schermer, E. R., Cembrano, J., Sanhueza, A., & McClelland, W. C. (1996). Geometry, kinematics and timing of intra-arc shear, southern Chile. *In: International Geological Congress, Proceedings, Beijing, China*, *1*, 214.

Sempere, T., Hérail, G., Oller, J., & Bonhomme, M. G. (1990). Late Oligocene-early Miocene major tectonic crisis and related basins in Bolivia. *Geology*, *18*(10), 946–949.

SERNAGEOMIN (2003). Mapa Geológico de Chile: versión digital. Servicio Nacional de Geología y Minería, Publicación Geológica Digital, No. 4 (CD-ROM, versión1.0, 2003). Santiago.

Siame, L. L., Bellier, O., Sébrier, M., & Araujo, M. (2005). Deformation partitioning in flat subduction setting: Case of the Andean foreland of western Argentina (28°S–33°S). *Tectonics*, *24*, TC5003. https://doi.org/10.1029/2005TC001787

Sielfeld, G., Lange, D., & Cembrano, J. (2019). Intra-arc crustal seismicity: Seismotectonic implications for the Southern Andes Volcanic Zone, Chile. *Tectonics*, *38*(2), 552–578.

Somoza, R. (1998). Updated Nazca (Farallon)-South America relative motions during the last 40 My: Implications for mountain building in the central Andean region. *Journal of South American Earth Sciences*, *11*(3), 211–215.

Sonder, L. J., Jones, C. H., Salyards, S. L., & Murphy, K. M. (1994). Vertical axis rotations in the Las Vegas Valley Shear Zone, southern Nevada: Paleomagnetic constraints on kinematics and dynamics of block rotations. *Tectonics*, *13*(4), 769–788.

Suárez, M., & Emparan, C. (1995). The stratigraphy, geochronology and paleophysiography of a Miocene fresh-water interarc basin, southern Chile. *Journal of South American Earth Sciences*, *8*(1), 17–31.

Suárez, M., & Emparan, C. (1997). Hoja Curacautín, Regiones de la Araucanía y del Bío-Bío. *Servicio Nacional de Geología y Minería, Carta Geológica de Chile*, *71*. ISSN 0716-0194

Taymaz, T., Yilmaz, Y., & Dilek, Y. (2007). The geodynamics of the Aegean and Anatolia: Introduction. *Geological Society of London, Special Publication*, *291*(1), 1–16. https://doi.org/10.1144/SP291.1

Thomson, S. N. (2002). Late Cenozoic geomorphic and tectonic evolution of the Patagonian Andes between 42°S and 46°S: An appraisal based on fission-track results from the transpressional intra-arc Liquine-Ofqui fault zone. *Geological Society of America Bulletin*, *114*(9), 1159–1173.

Torsvik, T. H., Müller, R. D., Van der Voo, R., Steinberger, B., & Gaina, C. (2008). Global plate motion frames: Toward a unified model. *Reviews of Geophysics*, *46*, RG3004. https://doi.org/10.1029/2007RG000227

Torsvik, T. H., Van der Voo, R., Preeden, U., Mac Niocaill, C., Steinberger, B., Doubrovine, P. V., et al. (2012). Phanerozoic polar wander, palaeogeography and dynamics. *Earth-Science Reviews*, *114*(3-4), 325–368.

Wallace, L. M., Beavan, J., McCaffrey, R., & Darby, D. (2004). Subduction zone coupling and tectonic block rotation in the North Island, New Zealand. *Journal of Geophysical Research*, *109*, B12406. https://doi.org/10.1029/2004JB003241

Wang, K., Hu, Y., Bevis, M., Kendrick, E., Smalley, R., Vargas, R. B., & Lauría, E. (2007). Crustal motion in the zone of the 1960 Chile earthquake: Detangling earthquake-cycle deformation and forearc-sliver translation. *Geochemistry, Geophysics, Geosystems*, *8*, Q10010. https://doi.org/10.1029/2007gc001721

Wang, K., Hu, Y., & He, J. (2012). Deformation cycles of subduction earthquakes in a viscoelastic Earth. *Nature*, *484*(7394), 327–332. https://doi.org/10.1038/nature11032

Zanettini, J. C. M., Leanza, H. A., Giusiano, A., Santamaría, G. R., & Franchi, M. (2010). *Hoja Geológica 3972-II Loncopué*. Provincia Del Neuquén: Segemar boletin n° 381 Buenos Aires 2010.

Zijderveld, J. D. (1967). A. C. demagnetization of rocks: Analysis of results. In D. W. Collinson, K. M. Creer, & S. K. Runcorn (Eds.), *Methods in Paleomagnetism, Dev. Solid Earth Geophys., vol. 3* (pp. 254–286). New York: Elsevier.